



Landslides as geological hotspots of CO₂ to the atmosphere: clues from the instrumented Séchilienne landslide, Western European Alps.

5 Pierre Nevers¹, Julien Bouchez², Jérôme Gaillardet^{2, 4}, Christophe Thomazo³, Laeticia Faure² and Catherine Bertrand¹

¹UMR Chrono-Environnement 16 route de Gray, 25000 Besançon, France

²Université de Paris, Institut de physique du Globe de Paris, CNRS, F-75005 Paris, France

10 ³UMR CNRS/uB6282 Biogéosciences 6 Boulevard Gabriel, 21000 Dijon, France

⁴Institut Universitaire de France, 75231 Paris, France

Correspondence to: Pierre Nevers (pierre.nevers@univ-fcomte.fr)

Abstract. This study makes use of a highly instrumented active landslide observatory (9 years of data) in the French Alps, the Séchilienne slope. Using a combination of major element chemistry and isotopes ratios (⁸⁷Sr/⁸⁶Sr, δ³⁴S) measured in
15 different water types of the stable and unstable part of the Séchilienne instability to assess the contribution of the different lithologies of the slope and the chemical weathering mechanisms. Chemical and isotopic ratios appear useful to characterize weathering processes and the origin of waters and their flowpaths through the massif. A mixing model allows us to allocate the different major elements to different sources and quantify the involvement sulfuric and carbonic acids as a source of protons.

20 As a consequence of the model, we are able to show that the instability creates favorable and sustained conditions for the production of sulfuric acid by pyrite oxidation by supplying reactive surfaces. We clearly identify the contribution of gypsum dissolution to the sulfate budget in the landslide. We are also able to refine the pre-existing hydrogeological views on the local water circulation and water flow paths in the instability but showing the hydrological connectivity of the different zones. Overall, our results show that the Séchilienne landslide, despite its role in accelerating rock chemical and
25 physical weathering, acts, at a geological time scale (i.e. at timescales longer than carbonate precipitation in the ocean) as a source of CO₂ to the atmosphere. If generalizable to other instable zones in mountain ranges, this study illustrates the complex coupling between physical and chemical erosion and climate. The study also highlights the importance of deciphering between sulfite oxidation and gypsum dissolution as a source of sulfate ions to rivers, particularly in mountain ranges.



30 1 Introduction

The weathering of rocks plays a key role in the chemical and climatic evolution of the Earth surface and is one of the geological processes that can impact atmospheric CO₂ concentration. When carbonic acid is the proton supplier, silicate weathering removes carbon dioxide from the atmosphere (Lerman et al., 2007, Berner and Berner, 2012). However, the oxidative dissolution of sulfides (*e.g.* pyrite FeS₂) produces sulfuric acid that can act as an alternative proton supplier to chemical weathering reactions. Although silicate weathering by sulfuric acid does not influence atmospheric CO₂, when sulfuric acid reacts with carbonate minerals, CO₂ is released towards the atmosphere (Lerman et al., 2007, Calmels et al., 2007, S.-L. Li et al., 2008, Torres et al., 2014). The relevance of this process for the global carbon cycle is two-fold. First, even though carbonate rocks constitute a minor fraction of the rock types exposed at the Earth surface, the dissolved products of carbonate dissolution dominate global weathering fluxes (Gaillardet et al., 1999) as they dissolve several orders of magnitude faster than silicates (Lasaga 1984). Second, because this process is limited by the supply of sulfide minerals to the Earth surface, it is particularly prominent in active mountain belts characterized by high erosion rates (Calmels et al., 2007; Torres et al., 2016; Blattmann et al., 2019). Within these tectonically active environments, landslides are likely to be hot-spots of sulfuric acid production, carbonate weathering, and CO₂ release (Emberson et al., 2015, 2018). Indeed, slope instability leads to sustained grain comminution and fractures opening, thereby providing a continuous supply of contact surfaces between water, air, and minerals that can in particular allow sulfuric acid production and carbonate mineral weathering (Binet et al., 2009; Bertrand et al., 2014).

Here we explore the idea that slope instability and associated deformation can constitute a mechanism that promotes coupled sulfide oxidation and carbonate weathering, in a contribution to the study of the role that active mountain ranges play on the global carbon cycle (Raymo and Ruddiman 1992). We focus on the Séchilienne slope instability located in the French Alps. This landslide serves as an observatory for landslide processes and has been the subject of many previous hydrogeological and geophysical investigations. This area offers the opportunity to study the role of erosion on sulfide oxidation and carbonate weathering under climatic conditions that differ from those of previous studies (such as Taiwan, the Himalayas, or the Andes), and thus to improve the knowledge on the global impact of landsliding on atmospheric CO₂ and climate. We combine measurements of the concentration of major elements and of the isotope composition of strontium and sulfur (⁸⁷Sr/⁸⁶Sr, δ³⁴S) dissolved in groundwater and springs to estimate the contribution of different rock types to the dissolved species produced by weathering reactions in the landslide. In particular, we estimate the relative role of different acid types (carbonic *vs.* sulfuric) and of two rock types (silicates *vs.* carbonates).

Besides bringing information on global impact of landsliding on atmospheric CO₂, Sr and S isotopes coupled to water chemistry brings significant progress in understanding the sources of solutes in natural waters and the chemical evolution of natural waters which allows us to improve existing hydrogeological model in complex environments such as landslides.



2 Study area

2.1 Geological setting

The "Séchilienne" site is a highly instrumented, and continuously monitored landslide, part of the French National Landslide Observatory (OMIV, <http://www.ano-omiv.cnrs.fr/>). The Séchilienne massif is located at the SW border of the Paleozoic crystalline Belledonne mountain range in the French Alps, 20 km southeast of Grenoble (Isère, France) (Fig. 1). The active zone of the site is a gravitational instability affecting $60 \cdot 10^6 \text{ m}^3$ of material, with a maximum depth of about 150 m, located on a south-facing slope of the massif (Le Roux et al. 2011). The most active part of the landslide, referred to as "les Ruines", is located on the eastern border of the unstable zone. Long-term monitoring (extensometers, geodetic measurements, tacheometers and microwave radar) has shown that its displacement velocity is estimated at 300 cm y^{-1} , while the less active parts of the site are moving at a mean of 10 cm y^{-1} (Le Roux et al. 2011; Dubois et al. 2014).

Geological, structural and information are provided by the geological map and by two boreholes drilled in 2010 in the unstable area at depths down to 150 m. Baudement et al. (2013) has integrated these information in a GOCAD® 3D model, recently used by Lajaunie et al. (2019) to propose a new vision of the Séchilienne slope based on a 3D resistivity model. The basement of the massif is mainly composed of micaschists showing a N-S trending sub-vertical foliation. Stratigraphically discordant deposits dating from the Carboniferous to the Liassic periods cover the micaschists on the top north – northeast of the massif (Mont Sec) and along the Sabot Fault. The slope is locally covered by Quaternary (Würm) glacio-fluvial deposits made of material reworked from the surrounding formations (Vengeon 1998, Vallet 2014). The micaschists consist primarily of quartz, biotite, phengite, and chlorite with the presence of carbonate veins and pyrite localized in fractures. These rocks also present small-scale variation in degrees of alteration, oxidation, and fracturation depending upon depth below surface, that can be related to different deformation and geochemical processes (Lajaunie et al. 2019). Carboniferous deposits are made of black shales, sandstones, and conglomerates with quartz and serpentine pebbles. Triassic rocks correspond to sandstone, quartzite, dolomite and locally of black shales, argillites, and gypsum. Liassic deposits are limestones with intercalation of layers rich in breccia consisting of micaschist, dolomite, and of coal (Barfély et al. 1972, Vengeon 1998, Vallet 2014). Strong local heterogeneities exist in terms of lithology and fracturation and are induced by the gravitational deformation (Lajaunie et al. 2019).

The part of the slope affected by the landslide extend from 400 m above sea level (a.s.l.) to 1100 m of altitude (Le Roux et al. 2011; Fig. 1d). Above the elevation of 1100 m a.s.l. the morphology of the Mont Sec corresponds to a plateau of glacial origin underlain by moraine deposits concentrated in small topographic depressions. The landslide is delimited at its northern border by a major head scarp of about 10 meters high and several hundreds of meters wide, which separates the glacial plateau of Mont Sec from the unstable zone. Eastward, N-S faults scarps limit the landslide whereas the western and southern parts are not well defined by geomorphological evidences. The motion of the landslide consists in a deeply rooted toppling movement with N50-70 slabs toward the valley, coupled with the sagging of the upper zone of the slope near the Mont Sec (Vengeon 1998). The Séchilienne instability is assumed to originate from the decompression of the basement



rocks after the Romanche glacier retreated at the last glaciation (15 kyr ago). Decompression caused the opening of fractures
 95 and then the collapse of the summit of the Mont Sec (Vengeon et al. 1999, Potherat and Alfonsi, 2001, Montjuvent and
 Winistorfer 1980). The Séchilienne slope is thus affected by a dense network of near vertical open fractures trending N70
 and N110/120, controlling the deformation of the Séchilienne landslide which is characterized by a deep progressive
 deformation (about 100-150m) and the absence of a well-defined basal sliding surface. Two N20 major fractures are also
 crossing the Séchilienne massif, the Sabot and the Séchilienne faults. Open fractures are locally filled with detrital material
 100 resulting from the erosion of the massif (Vallet et al. 2015a).

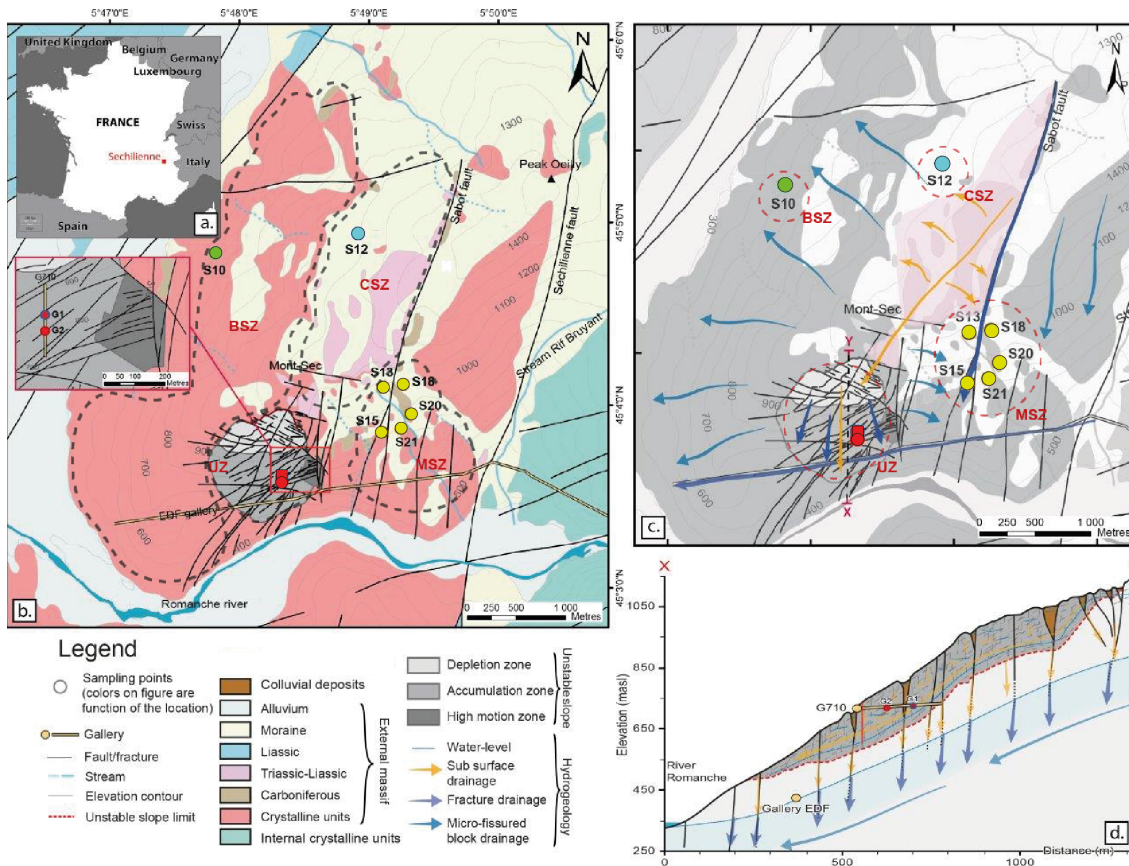


Figure 1: Map of the Séchilienne site a. location of the Séchilienne massif in the French Alps, b. Simplified geological map of the Séchilienne massif and sampling locations, c. schematic hydrogeological model of the Séchilienne massif, d. hydrogeological cross-section of the instability, modified after Vallet et al. (2015).

105



2.2 Hydrogeological setting

The high degree of fracturation of the massif and its heterogeneity lead to distinct and complicated hydrological flow paths, characterized by different transit times related to a dual permeability behavior that is typical of fractured rock aquifers where

110 conductive fractures play a major role in the drainage (Fig 1.c). Two main groundwater flow types are identified: a rapid transit through fractures, and a more inertial circulation through the micro-fissured, less permeable rock matrix (Maréchal 1998, Cappa et al. 2004, Vallet et al. 2015a). The Sabot and Séchilienne faults play an important role on fluid flow through the massif by draining waters from the sedimentary cover at a fast rate (0.7 km.day^{-1}), and bypassing the less pervious and more inertial micro-fissured matrix characterized by lower flow velocity (0.08 km.day^{-1}) (Mudry et Etievant 2007).

115 Regarding the rest of the massif, besides fractures, groundwater flow is more inertial and is characterized by a longer residence time (Vallet et al. 2015a). Local perched aquifers develop during high flow periods and discharge downwards to the main aquifer, due to the contrast of permeability between the decompressed zone at the surface and the unaltered rock (Lajaunie et al., 2019). The gallery built by Électricité de France (EDF), located at the base of the slope, acts as a major westward drain for groundwater (Vallet et al. 2015a).

120 Difference in hydraulic conductivity between the highly fractured unstable zone (thickness about 150-200 m, Le Roux et al. 2011) and the basement situated under the landslide (Fig 1.d) led to the build-up of a two-layer aquifer system. Those two aquifers are connected to one another through major fractures (Vengeon 1998, Meric et al. 2005; Le Roux et al. 2011, Guglielmi et al. 2002, Vallet et al. 2015a). A temporary and discontinuous shallow perched aquifer is present in the landslide with extension and connectivity varying according to short-term recharge variations. This aquifer is almost dry during the

125 low flow periods, with numerous disconnected saturated pockets (such as open fractures filled by colluvial deposit and altered material) linked to the heterogeneity of the landslide (Guglielmi 2002, Cappa et al. 2004, Vallet et al. 2015a). The recharge of this aquifer is mainly local (through trenches and counterscarps, limiting the runoff) with a contribution of remote groundwater through near-surface drainage at high-flow periods from the sedimentary cover above the landslide (near the Mont Sec summit) (Guglielmi 2002, Vallet et al. 2015a). The deep aquifer, which extends all over the massif

130 (altitude close to 550 m asl), corresponds to a saturated layer hosted by the fractured metamorphic bedrock and to an overlying, 100-m thick vadose layer (Vallet et al. 2015a). The deep aquifer level is controlled by the constant water heads of the Romanche alluvium in the valley, and of the EDF gallery (425 m a.s.l.).

3. Samples and analytical methods

Nine outflows draining the whole massif were investigated for physico-chemical parameters and dissolved load chemistry

135 (Fig 1.a). Two of these outflows (G1 and G2) are located within the Unstable Zone (UZ), and correspond to seep water collected in a gallery excavated to monitor the landslide at 710 m a.s.l. (G710). The remaining outflows (S10, S12, S13, S15, S18, S20, S21) correspond to springs draining the Stable Zone (Fig 1.a). These outflows can be differentiated regarding the dominant local lithology: S10 is located in the Bedrock Stable Zone (BSZ), S12 in the Carbonate Stable Zone (CSZ), and



S13, S15, S18, S20, and S21 are located in an area of the Stable Zone characterized by mixed lithology (Mixed Stable Zone, MSZ). Samples were collected every three months over the period 2010-2019. Between 2014 and 2017, waters were sampled once a year for Sr isotopes, while samples for S isotope were collected in 2019. In total, 360 water samples were collected and analyzed for this study.

Field measurements of water temperature, pH, and electrical conductivity (EC) were made with a WTW pH/Cond 340i (Xylem Inc.) sensor, with a precision of 0.1 unit and $0.1 \mu\text{S cm}^{-1}$ for pH and EC, respectively.

Water samples were collected in polyethylene bottles and filtered with a $0.45 \mu\text{m}$ pore diameter nylon filter, before being preserved in cold conditions for measurements of major element concentration and Sr and S isotopes.

Analyses of dissolved major elements were all carried out at the research laboratory Chrono-Environnement at the University of Franche-Comté. Dissolved major cation concentrations were measured by atomic absorption spectrometry (AA 100 Perkin-Elmer) with detection limits of 0.5, 0.1, 0.01, and 0.1 mg L^{-1} for Ca^{2+} , Mg^{2+} , Na^{+} and K^{+} , respectively. Dissolved anion concentrations were determined using high-pressure ion chromatography (Dionex DX 100) with detection limits of 0.1, 0.1, and 0.05 mg L^{-1} for Cl^{-} , SO_4^{2-} and NO_3^{-} , respectively. The concentration of HCO_3^{-} was measured by acid titration ($\text{N}/50 \text{ H}_2\text{SO}_4$) within 48 hours after sampling, with 1% accuracy. Dissolved silica concentration was analyzed with a spectrophotometer (Spectroquant, Pharo 300, Merck) using a silica-test kit (Merck) with 3% accuracy. Only analyses with a charge balance better than 10% were taken into account.

Water and rock samples were collected for Sr isotope ($^{87}\text{Sr}/^{86}\text{Sr}$ ratio) analyses. Rocks have been sampled in four different lithologies encountered among the slope: basement micaschist, carbonate and dolomite from the sedimentary cover, recrystallized calcite vein in micaschist. Strontium isotope analyses were carried out at High-Resolution Analytical Platform (PARI) of the Institut de physique du Globe de Paris (IPGP). For water samples, dissolved Sr was first isolated from the water sample matrix by automated ion chromatography following the method of Meynadier et al. (2006). In addition to bulk samples analysis, a three-step sequential leaches was conducted using H_2O , 1M acetic acid and 1M HCl. The first step is designed to recover the exchangeable fraction adsorbed onto the solid surface; step 2 was for extracting Sr from carbonates, amorphous hydroxides, and phosphate minerals (Tessier et al., 1979); step 3 was to dissolve any high-order Fe–Mn oxide/oxyhydroxide phases that might be present after HCl leaching (Tessier et al., 1979). The leachate solutions and residual samples were processed for $^{87}\text{Sr}/^{86}\text{Sr}$ ratio analysis following the same procedure used for bulk samples. Bulk digestion of samples was conducted using concentrated HF and HNO_3 acids. For rock samples, 3M HNO_3 aliquots of digestion solutions were loaded on columns loaded with 0.2 mL of Sr-SPEC resin (Eichrom). Then, 3M HNO_3 was used to elute the sample matrix before Sr was eluted in H_2O . Strontium isotope ratios were then measured using a Multi-Collector Inductively Coupled Plasma Mass Spectrometer (MC-ICP-MS; Thermo-Fisher Neptune) in low resolution mode (Hajj et al., 2017). Purified Sr solutions were introduced using an APEX desolvation unit and a PFA nebulizer at a rate of 50 to $100 \mu\text{L min}^{-1}$ depending on the measurement session, and at Sr concentrations between 50 and 150 ppb. The accuracy and reproducibility of the $^{87}\text{Sr}/^{86}\text{Sr}$ analysis was assessed using repeated measurements of the international isotope Sr carbonate standard (SRM987, NIST). The obtained values for SRM987 standard NIST was 0.710249 ± 0.000025 .



Sulfur isotopes measurements were performed at the Biogéosciences Laboratory, University of Bourgogne, Dijon, France on both sulfates from water samples (Table A1) and sulfides from basement micaschist (Table B2).

175 Nine samples were treated with an excess of 250 g l⁻¹ BaCl₂ solution to precipitate BaSO₄. After centrifugation, the BaSO₄ precipitate was washed several times with deionized distilled water and dried at 60°C for 24 hours in an oven. Five hundred micrograms of purified barite samples were poured into tin capsules and homogeneously mixed with 1/3 of vanadium pentoxide before isotopic measurements (³⁴S, ³²S) using a Vario PYRO cube (Elementar GmbH) connected online *via* an open-split device to an IsoPrime IRMS system (Isoprime, Manchester, UK). Sulfur isotope data are expressed in delta

180 notation and reported in units per mille (‰). The δ³⁴S data are reported with respect to the international standard Vienna Cañon Diablo Troilite (VCDT). Analytical errors are ±0.3‰ (1σ) based on replicate analyses of the international barite standard NBS-127, which was used for data correction assuming a δ³⁴S value of +20.3 on the VCDT scale

Sulfides sulfur extractions from rocks of the basement micaschist formation were carried out on 3 grams of 8 samples (4 sub-samples on each of two rock samples, including unaltered pyrite and iron oxides; Table B2) following the method described

185 by Canfield et al. (1986). Dried and rinsed Ag₂S precipitates recovered after wet chemistry sulfides extraction are weighted for gravimetric quantification of sample sulfur content. Five hundred micrograms of silver sulfides precipitates were then mixed with an equivalent weight of tungsten trioxide in tin capsules before combustion in a Vario pyro cube (Elementar GmbHTM). Sulfur isotope compositions (δ³⁴S) were measured using an IsoPrime IRMS device (Isoprime, Manchester, UK). International standards (IAEA-S-1, IAEA-S-2, IAEA-S-3) were used for calibration and results are reported in the δ-notation

190 relative to the Vienna Canyon Diablo Troilite (VCDT) standard. Reproducibility (1σ) is better than 0.2‰ based on duplicate analyses of standard materials and samples.

4. Results

The concentration of major elements, EC, pH, temperature and Sr and S isotope composition of water samples are given in Table A1.

195 4.1 Major dissolved elements

The chemical composition of waters sampled on the Séchilienne site is very diverse, reflecting heterogeneity in rock types and the existence of various groundwater flow paths. Water pH in Séchilienne is relatively high and varies from 6.5 to 9.4 with a mean value of 7.9. Electrical conductivity range between 79 μS cm⁻¹ and 1114 μS cm⁻¹ (Table A1). From the major ion perspective, samples can be grouped into 4 main water types (Fig. 2). These water types correspond to those identified

200 previously by Vallet et al. (2015a). Type 1 corresponds to Ca-HCO₃ waters, typical of water draining carbonate formations, typified by the S12 spring draining the carbonate cover at the top of the Séchilienne slope (CSZ). S12 has low EC values ranging from 79 μS cm⁻¹ to 147 μS.cm⁻¹ with a mean of 117 μS cm⁻¹. The second group corresponds to Mg-Ca-HCO₃ rich waters, which have circulated through the sedimentary cover (carbonate and dolomite) and the micaschists bedrock and is



represented by the S10 spring (BSZ). All S10 samples have higher electrical conductivities ranging from to 308 $\mu\text{S cm}^{-1}$ to
205 509 $\mu\text{S cm}^{-1}$ with a mean of 443 $\mu\text{S cm}^{-1}$. Waters sampled in the unstable part of the slope (UZ), include the underground
outflows G1 and G2 and show a chemical composition that vary from Mg-Ca-HCO₃-SO₄ waters to Mg-Ca-SO₄ waters and
constitute the third hydrogeochemical group. The highest EC values of this study are observed for the G1 outflow with
electrical resistivities ranging from 613 $\mu\text{S.cm}^{-1}$ to 1114 $\mu\text{S.cm}^{-1}$ with a mean value of 824 $\mu\text{S.cm}^{-1}$. The other outflow of the
unstable zone (outflow G2), in contrast to the previous one, shows a mean electrical conductivity value around 391 $\mu\text{S.cm}^{-1}$,
210 with a minimum value of 313 $\mu\text{S cm}^{-1}$ (and a maximum value of 470 $\mu\text{S cm}^{-1}$). The fourth and last type of waters include the
S13, S15, S18, S20, S21 outflows, sampled in the stable part of the slope (MSZ) along the Sabot fault, and show Ca-Mg-
HCO₃-SO₄ type waters. The MSZ group exhibits EC values ranging from 357 $\mu\text{S cm}^{-1}$ to 567 $\mu\text{S cm}^{-1}$, with a mean of 479
 $\mu\text{S.cm}^{-1}$. In addition to these spring samples, rainwaters samples (Table A1) show very low EC values with a mean of 26 μS
 cm^{-1} and low concentrations for all elements analyzed. In particular, chloride concentrations range from 3.3 $\mu\text{mol L}^{-1}$ to 20.3
215 $\mu\text{mol L}^{-1}$.

Waters of the Unstable Zone group (G1,G2) are characterized by the highest concentrations in SO₄²⁻ (from 1.32 to 3.90
mmol.L⁻¹) compared to the other outflows sampled which have values ranging from 0.57 to 1.34 mmol.L⁻¹ for the MSZ
outflows (S13, S15, S18, S20, S21) and from 0.48 to 0.67 for the S10 (BSZ) outflow (Fig. 2; Table A1). Fig. 2 clearly shows
that SO₄²⁻ ions are significantly contributing the electrical balance of the analyzed waters.

220

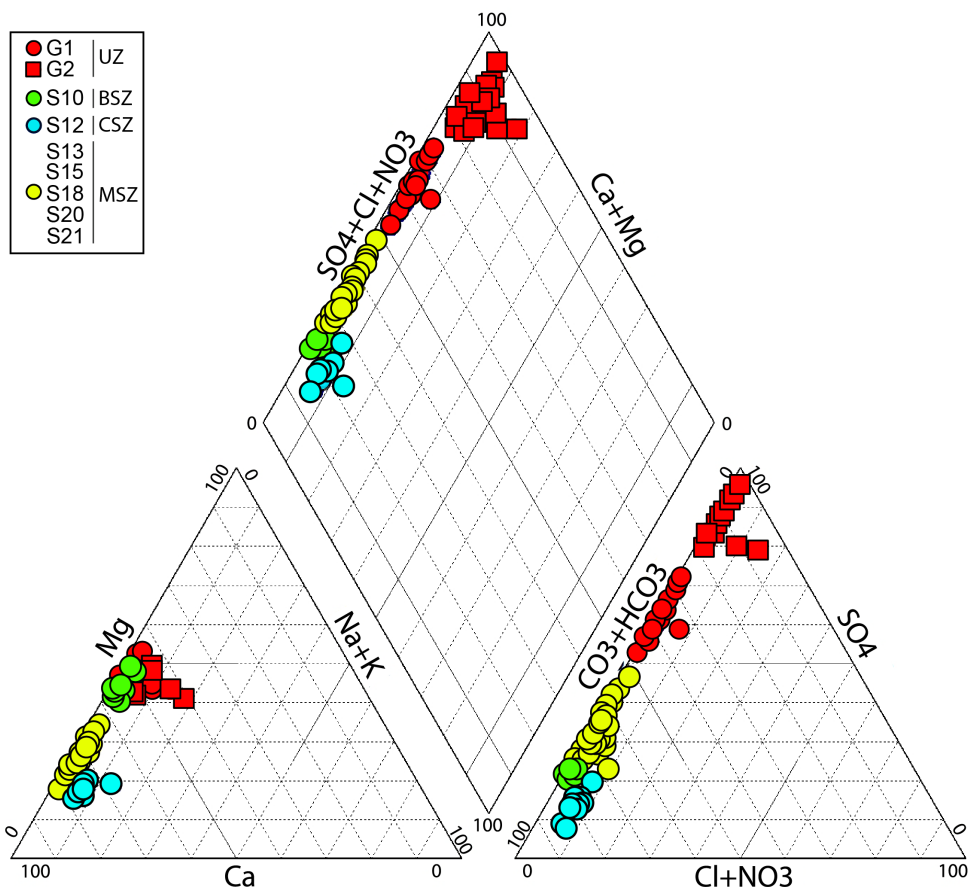


Figure 2: Piper diagram representing the major water types samples in the outflows of the Séchilienne massif

4.2 Strontium isotopes

225 *Rock samples*

The highest $^{87}\text{Sr}/^{86}\text{Sr}$ ratios were found in the micaschists samples with a value of 0.7351 (Table B1), typical of silicate rocks ($0,73\pm 0,01$; Négrel et al., 1993). The calcite veins contained in the micaschists also show high Sr isotopic ratios (0.7277). By contrast, carbonate rocks have lower Sr isotopic ratios, with the lowest value being 0.7095 slightly higher than the Sr isotopic composition of lower Jurassic seawater (from 0.7065 to 0.7076; Koepnick et al., 1990). Intermediate values of 0.7106 are found for of the Laffrey sedimentary cover having an age similar to that of the carbonates, possibility indicating diagenetic alteration of the original seawater signal.

230

Spring water samples



The Sr isotope ratios measured in the spring samples in and around the Séchilienne instability range from 0.7093 to 0.7231
235 (Table A1). The four main groups of waters have contrasted $^{87}\text{Sr}/^{86}\text{Sr}$ isotopic ratios. The highest $^{87}\text{Sr}/^{86}\text{Sr}$ values are found
in the UZ underground outflows samples (G1, G2) with an average of 0.7210 (S.D: 0.00056). The lowest $^{87}\text{Sr}/^{86}\text{Sr}$ values
correspond to the waters of the MSZ (springs S13, S15, S18, S20, and S21), and average at 0.7095 (S.D: 0.00012), *i.e.* at the
value measured in the carbonate rock. The S12 outflow (CSZ) is characterized by $^{87}\text{Sr}/^{86}\text{Sr}$ ratios of around 0.7095 (S.D:
0.70952), *i.e.* close to those of the MSZ group. Intermediate values of Sr isotopic ratios are found for the samples of the BSZ
240 group (S10), with an average of 0.7148 (S.D: 0.00019).

4.3 Sulfur isotopes

Rock samples

Sulfur isotope composition of unaltered rock samples range from -7.9‰ to 17.8‰ with an average value of 1.23‰ (S.D:
11.82), whereas weathered micaschists exhibit $\delta^{34}\text{S}$ values ranging from -13.1 to 9.9‰ and an average of -1.42‰ (S.D: 9.55)
245 (Table B2). These numbers show the extremely large range of possible sulfur isotope signals co-existing in the various rock
types present in the landslide.

Spring water samples

Waters show a much narrower range of $\delta^{34}\text{S}$ values, ranging from -5.5‰ to 6.5‰ (mean 0.43‰, S.D: 5.12). The highest $\delta^{34}\text{S}$
250 values are observed for water of the MSZ group (outflows S13, S15, S20, S21) with an average of 6.28‰ (S.D: 0.3381).
Samples of the S12 outflow (CZS group) also exhibits a high $\delta^{34}\text{S}$ value of 6.03‰. The G1 and G2 outflows (UZ group)
exhibit negative $\delta^{34}\text{S}$ values with an average of -3.74 ‰ (S.D: 1.7473), with lower $\delta^{34}\text{S}$ values for G2, (averaging at -5.33‰
; S.D: 0.2191) than for G1 (mean: -2.2‰ ; S.D: 0.0652). The BSZ group (outflow S10) is characterized by $\delta^{34}\text{S}$ values that
are intermediate between those of the MSZ and UZ groups (2.4 ‰).

255 5. Discussion

5.1 Identification of sources to dissolved species

5.1.1 Atmospheric and anthropogenic sources

Rainwater is potentially a significant source of elements to the water sampled in the different springs at Séchilienne. To
assess the importance of atmospheric inputs, we use Cl^- concentrations. Chloride is not significantly involved in chemical
260 reactions at the Earth surface and its presence in waters has three main origins: rainwater (through the dissolution of seasalt
aerosols), dissolution of saline rocks, and anthropogenic inputs. As the presence of chloride-bearing saline rocks in the
studied area has not been reported, anthropogenic and rain inputs are likely to be the major sources of Cl^- . The expected
concentration of Cl^- derived from precipitation in spring waters (hereafter called $[\text{Cl}]_{\text{crit}}$ for "critical chloride", Stallard et al.,

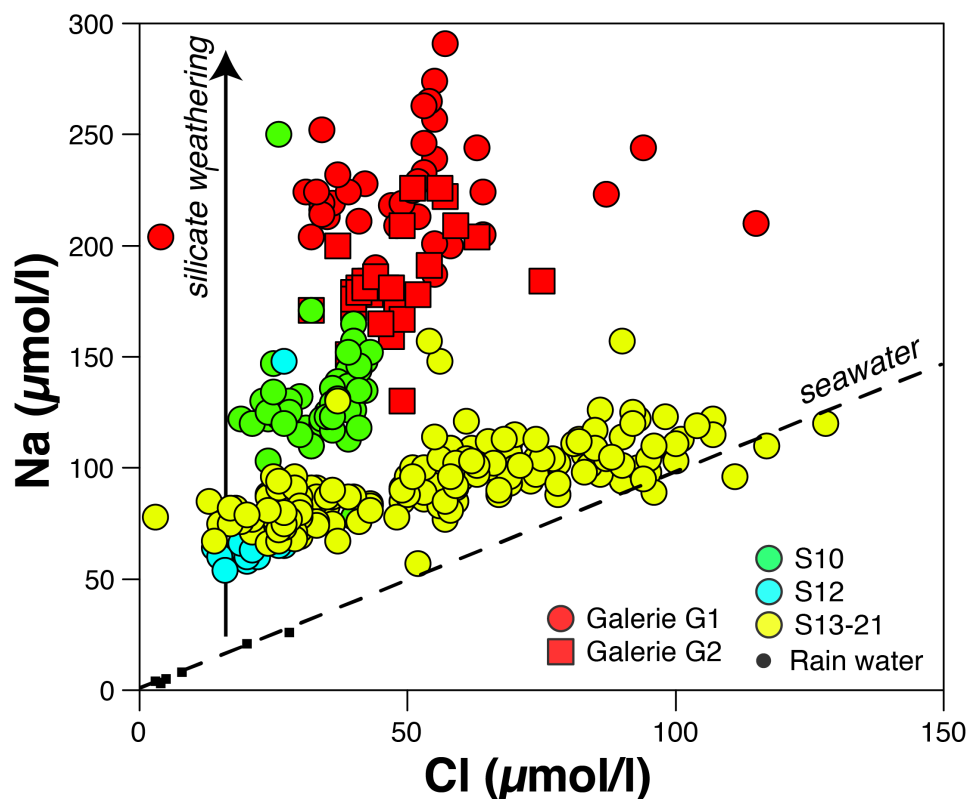


1983) of the Séchilienne massif can be estimated by multiplying the mean Cl^- concentration found in rainwater by the mean
265 evapotranspiration factor (P/ETP : 4.02 with P : precipitation, ETP : evapotranspiration calculated from temperature and
latitude of the study site, according to Oudin et al. 2005). Alternatively, $[\text{Cl}]_{\text{crit}}$ can be estimated as being equal to the lowest
 Cl^- concentrations in the sample set (S10, S12 and S21 springs). Both methods concur to fix the atmospheric contribution of
 Cl^- to the Séchilienne waters at a maximum of $30 \mu\text{mol l}^{-1}$. Above this concentration, additional sources must be involved.
Significant excess of Cl^- ($[\text{Cl}] > [\text{Cl}]_{\text{crit}}$) is found for the G1 and G2 underground outflows (between $15\text{-}20 \mu\text{mol l}^{-1}$ of
270 excess), as well as in the S15, S20, and S21 springs where this excess is the highest (about 30 to $60 \mu\text{mol l}^{-1}$). Excess Cl^-
concentrations of springs S13-S21 show a significant correlation with NO_3^- concentrations ($R^2 = 0.65$, not shown). As NO_3^-
can only have an anthropogenic origin, this correlation supports the idea that the origin of the Cl^- excess in springs S13-S21 is
most probably added by domestic and/or agricultural activities. The excess of Cl^- in the underground outflows G1 and G2 is
more difficult to explain. We attribute this excess either to infiltration of surface waters contaminated by anthropogenic
275 activities, and/or to the release of Cl^- from present in the rocks of the Unstable Zone.

Once $[\text{Cl}]_{\text{crit}}$ is known, it is possible to correct all cation concentrations from the atmospheric seasalt input by using:

$$[X]^* = [X] - [\text{Cl}]_{\text{crit}} \times \left(\frac{X}{\text{Cl}}\right)_{\text{seawater}} \quad (1)$$

280 In this equation, $[X]^*$ denotes the concentration of an element X in the water sample, corrected from the atmospheric input,
and $(X/\text{Cl})_{\text{seawater}}$ is the seawater elemental ratio. This correction is only significant for Na^+ , due to the relatively high
concentrations found in the Séchilienne waters.



285 Figure 3: Na vs Cl concentrations measured in the different groups of water outflow from the S chilienne massif. Rainwater data points are aligned along the seawater composition (seasalts). Na^* is defined as the difference $Na - Cl_{crit}$ where $Cl_{crit} = 30 \mu mol/l$ (see text) where Cl_{crit} is the concentration of chloride only derived from rainwater and concentrated by evapotranspiration.

5.1.2 The importance of silicate weathering in S chilienne

290 The concentration of Na^+ , once corrected from atmospheric input (Na^*) using equation (1), is a proxy of silicate weathering reactions, as the only remaining significant source of Na in surface waters is the dissolution of silicate minerals. The underground outflows G1 and G2 have the highest Na^* concentrations (mean values $200 \pm 30 \mu mol l^{-1}$ and $158 \pm 21 \mu mol l^{-1}$ for G1 and G2 respectively) (Fig. 3). This confirms the importance of silicate weathering reactions in the Unstable Zone, made of fractured micaschists. Although the source of excess chloride could also be contributing Na (were this additional source NaCl inclusions), the Na^* concentrations remain the highest found in the S chilienne landslide area even after
295 correcting for an amount of Na equals to $[Cl] - [Cl]_{crit}$. Despite their excess of Cl, the MSZ outflows chemistry also reveals that silicate weathering reactions are releasing Na^+ to those waters (Fig. 3). However, the Na^* concentrations of the Mixed Stable Zone ($60 \mu mol/l$ on average) are equal to around half of those encountered in the Unstable Zone. This contrast between the stable (MSZ) and unstable zone (UZ) illustrates that at S chilienne the importance of silicate weathering is



300 linked to the fracturation degree. Finally, the low Na* concentration in the S12 outflow (Fig. 3) can be attributed to the fact that it mainly drains the carbonate cover. The most plausible explanation for the non-zero Na* concentration in S12 is the release of Na from clays disseminated in the carbonate rocks.

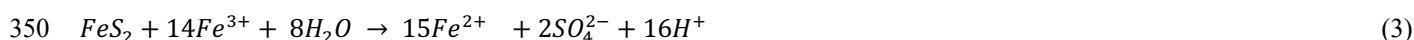
5.1.3 Identifying sources to solutes in the springs of the Séchilienne massif

In the following we use dissolved elemental and isotopic ratios to constrain the rock sources (silicates, carbonates, and gypsum) of the solutes in the Séchilienne springs. As shown above, strong contrasts exist in $^{87}\text{Sr}/^{86}\text{Sr}$ ratios between the sedimentary carbonate cover and the crystalline rocks of the basement. The isotopic ratio of dissolved Sr released by water-rock interaction reflects that of the minerals that dissolve and is not affected by the reincorporation of Sr in secondary minerals (e.g. Negrel et al. 1993). Sr isotopes can thus be used to trace the provenance of dissolved Sr, and by extension of the different cations, in the waters of Séchilienne. By contrast, elemental ratios such as Ca/Sr and Mg/Sr may be affected by the precipitation of secondary minerals and in particular by the formation of secondary carbonates (Bickle et al., 2015) and should be used more carefully to identify the provenance of cations.

A series of plots using $^{87}\text{Sr}/^{86}\text{Sr}$ as a common Y axis are shown in Fig. 4. $^{87}\text{Sr}/^{86}\text{Sr}$ vs. Ca/Sr or Na/Sr plots (Fig. 4a and 4b) conservative mixing between reservoirs is indicated by straight lines joining the endmembers. The Ca/Sr ratios for the carbonate, silicate, and evaporite endmembers are taken from Negrel et al. (1993) and Gaillardet et al. (1997). The corresponding Sr isotopic ratios are those measured in the rock samples from the Séchilienne massif (Table B1). The location of data points corresponding to springs S13, S15, S18, S20, S21 (MSZ group) in Fig. 4a and 4b shows that their relatively low Sr isotopic composition can not only be derived from the dissolution of carbonates. A second unradiogenic endmember contributing with low Ca/Sr and Na/Sr ratios needs to be invoked. As indicated by Fig. 4c this endmember is enriched in sulfate as shown by its high SO_4/Na ratio. Although gypsum outcrops are not visible at the Séchilienne slope, gypsum is clearly known to exist in the local Triassic formations lying in the upper part of slope as indicated by the regional geological map (Fig.1). Gypsum is also well known in the Triassic strata of the external Alps where it plays a major role in deformation and thrusting (Barf  ty et al. 1972). The occurrence of gypsum and carbonate dissolution endmembers inferred from the chemistry of the Séchilienne springs indicates that the Sabot Fault which lies at the North-East of the MSZ outflows (Barf  ty et al. 1972) plays a major role in draining aquifers hosted by sedimentary rocks to the MSZ and BSZ outflows. The Sr and S isotope composition of Triassic seawater (between 0.7075 and 0.708 and $15\pm 3\%$, respectively; Burke et al. 1982, Fanlo and Aroya 1998, Kampschutte and Strauss 2004) and the Ca/Sr ratio of waters draining gypsum (Gaillardet et al., 1997; Meybeck et al., 1986) are entirely consistent with the contribution of gypsum dissolution. Fig. 4 also shows first that the S12 spring, identified by Vallet et al. (2015a) as characterized by rapid flowpaths through the sedimentary cover, in addition to being less mineralized than the MSZ group, is not influenced by gypsum dissolution despite its geographical position on the sedimentary part of the slope. The relatively high Na/Sr ratios observed in the S10 spring is probably due to an anthropogenic influence, as revealed by the high nitrate concentrations measured in this spring.

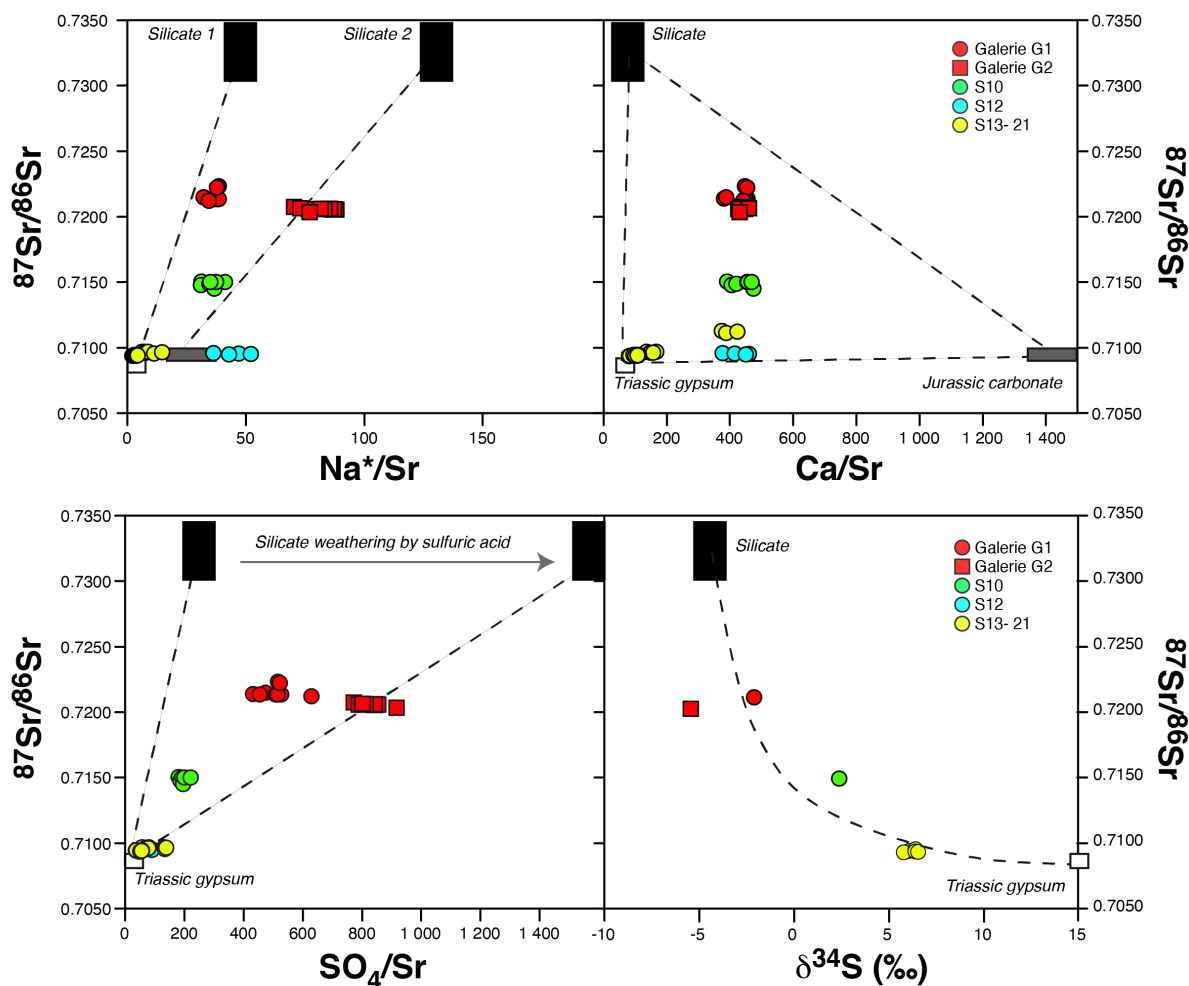


By contrast, waters from the UZ outflows (G1, G2) present $^{87}\text{Sr}/^{86}\text{Sr}$ and chemical ratio values clearly influenced by a silicate endmember. However, their Sr isotopic signature is lower than those of local micaschist, indicating the additional contribution of Sr from a carbonate or evaporitic source to the G1 and G2 spring (Fig. 4a). The $^{87}\text{Sr}/^{86}\text{Sr}$ ratios of waters of the S10 outflow also exhibit intermediate values between the silicate and carbonate-gypsum mixing line, but with $^{87}\text{Sr}/^{86}\text{Sr}$ ratio lower than those of the UZ outflows, supporting the idea that water-silicate interaction in the BSZ were less intense than in the UZ. These conclusions based on Sr isotopes are in full agreement with those made from Na^* concentration above and can be interpreted as reflecting the lesser degree of fracturation of the stable zone compared to the unstable zone. Fig. 4c and Fig. 4d show that the higher $^{87}\text{Sr}/^{86}\text{Sr}$ ratios observed in springs of the UZ (G1, G2), and to a lesser extent of the BSZ (S10) are associated with sulfate enrichment. However, unlike for samples of the MSZ (S13-S21), dissolved sulfate in UZ and BSZ samples has a relatively low S isotope composition (Fig. 4d). This observation is compatible with a significant influence of sulfide oxidation, despite the very wide range of $\delta^{34}\text{S}$ values measured in the bedrock micaschists (between -13,14‰ and 17,77‰, average -0,10‰, S.D: 10,05; Table B2). The presence of pyrite has clearly been reported in the unstable zone of Séchilienne (Bertrand et al. 2014, Vallet et al. 2015a). The concomitant increase in SO_4^{2-} and radiogenic Sr (Fig. 4c), combined with the decrease in $\delta^{34}\text{S}$ (Fig. 4d) suggests a coupling in the unstable zone between sulfide oxidation and silicate weathering. The oxidative weathering of pyrite, possibly by O_2 or water, can then release sulfate to waters (e.g. Spence and Telmer, 2005):



The oxidation of sulfide to intermediate sulfur species or to sulfate appears to produce only small isotope effects (Fry et al., 1986, 1988; Zerkle et al., 2009; Balci et al., 2012). The significance of these reactions in the unstable zone of Séchilienne can be related to the role of fracturation and grain comminution in favoring the contact between water, air, and minerals through which is the rate-limiting factor for a fast-chemical reaction such as pyrite oxidation.

Altogether, our analysis shows that the composition of the water outflows from the Séchilienne site can be interpreted by a variable contribution of waters having interacted with micaschists and sedimentary rocks, and by a dual origin (sulfide oxidation and gypsum dissolution) of sulfate ions. The chemical and isotopic characteristics of the MSZ and UZ waters shows that they have percolated through the sedimentary cover before reaching their outlet in the massif through the Sabot fault.



365 Figure 4: Sr isotopic composition of the different groups of water outflow from the Séchilienne massif as a function of Sr-normalized ratios (a, b and c) and S isotopic composition. Mixing endmembers are discussed in the text (Table C1). Straight lines indicate a mixing process in Fig. 4a, 4b and 4c. In Fig. 4c, the dashed line is a mixing hyperbola calculated based on the composition of the endmembers ($^{87}\text{Sr}/^{86}\text{Sr}$, $\delta^{34}\text{S}$, and SO_4/Sr ratios of the silicate and carbonate endmembers).

5.1.4 Quantitative apportionment

370 The use of Sr isotopes and major elements makes it possible to estimate the proportions of the different base cations in each identified endmember. The details of these calculations are given in Appendix. Following the above discussion of the mixing endmember, the following equations can be written:

$$\left(\frac{^{87}\text{Sr}}{^{86}\text{Sr}}\right)_{\text{mix}} = X_{\text{sil}}^{\text{Sr}} \cdot \left(\frac{^{87}\text{Sr}}{^{86}\text{Sr}}\right)_{\text{sil}} + X_{\text{carb}}^{\text{Sr}} \cdot \left(\frac{^{87}\text{Sr}}{^{86}\text{Sr}}\right)_{\text{carb}} + X_{\text{gyyps}}^{\text{Sr}} \cdot \left(\frac{^{87}\text{Sr}}{^{86}\text{Sr}}\right)_{\text{gyyps}} \quad (4)$$



$$\left(\frac{Na}{Sr}\right)_{mix} = X_{sil}^{Sr} \cdot \left(\frac{Na}{Sr}\right)_{sil} + X_{carb}^{Sr} \cdot \left(\frac{Na}{Sr}\right)_{carb} + X_{gyyps}^{Sr} \cdot \left(\frac{Na}{Sr}\right)_{gyyps} \quad (5)$$

$$375 \quad 1 = X_{sil}^{Sr} + X_{carb}^{Sr} + X_{gyyps}^{Sr} \quad (6)$$

Where the subscripts mix, sil, carb and gyyps denote the mixture (water), the silicate, carbonate and gypsum endmembers respectively. Proportions of Sr derived from each of those endmembers i are denoted X_i^{Sr} . All ratios are corrected from atmospheric inputs according to the above method. Because the carbonate and gypsum endmember add relatively few Na
 380 compared to Na* (Na from silicates), equation 5 simplifies into:

$$\left(\frac{Na}{Sr}\right)_{mix} = X_{sil}^{Sr} \cdot \left(\frac{Na}{Sr}\right)_{sil} \quad (7)$$

This assumption is supported by the positions of the different springs in Fig. 4b, which indicates that the low-⁸⁷Sr/⁸⁶Sr
 385 component, encompassing both carbonate and gypsum weathering of the springs has a negligible Na content. The proportions of Sr in the different mixing reservoirs can then be estimated and the contribution of each of these end members to the load of the dissolved major species SO₄, Ca, and Mg then calculated. This can be calculated from the contributions to dissolved Sr following:

$$390 \quad X_i^E = X_i^{Sr} \left(\frac{E}{Sr}\right)_i / \left(\frac{E}{Sr}\right)_{spring} \quad (8)$$

with $i = sil, carb, \text{ or } gyp$, and $E = SO_4, Mg, \text{ or } Ca$ (corrected from rain inputs). Full discussion on the choice of the $(Na/Sr)_{sil}$ and of the $(E/Sr)_i$ ratios is given in Appendix C.

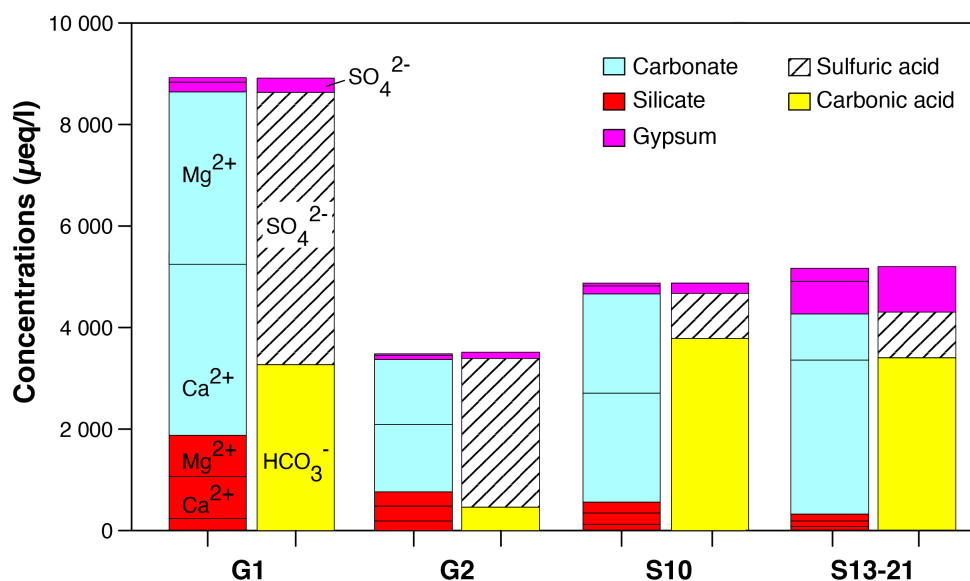
A Monte Carlo approach was used, in order to quantify uncertainty. Results are given in Table C2 and represented in figure
 395 5 as an histogram. Proportions are reported as the median value (50%)[±] s.d. Carbonate dissolution appears as the main contributor of all the waters sampled on the different parts of the studied zone (UZ, BSZ, MSZ) (Table C2; Fig. 5). In the most active part of the landslide (G1, G2), despite the silicate-dominated lithology, silicate endmember contribution is lower than carbonate contribution, indicating the waters percolating through the unstable zone acquired part of their chemical and isotopic composition from above the hillslope. Calculations of the proportions of sulfate derived from the different
 400 endmembers show a minor but non negligible contribution of gypsum dissolution and a very clear contribution of pyrite oxidative weathering particularly important in the fractured zone. In G2 group, most of the anions are provided by the oxidative weathering of pyrite. BSZ exhibit a lower proportion from silicate endmember with a median of 0.11%_{0.11}^{0.12} for BSZ and 0.21%_{0.19}^{0.22}, 0.22%_{0.21}^{0.24} respectively for G1 and G2. This difference is justified by the unstable context of G1 and G2 weathering destabilization and weathering are higher than the stable part of the slope at the BSZ outflow.



405 In waters of the MSZ (S13-S21), significant contribution of gypsum is evidenced in the results of the mixing equations with values ranging between $0.13\%_{0.05}^{0.27}$ and $0.23\%_{0.09}^{0.40}$. These values agree with the correlation presented in Fig. 4d. Even if we do not attribute much confidence to the mixing proportions derived from the correlation of Fig. 4d, due to the uncertainties of the pyrite endmember, we consider it as a qualitative proof that sulfur in the Séchilienne waters are derived essentially from pyrite oxidation in the unstable zone, from gypsum dissolution the MSZ waters (S13, S15, S18, S20, S21).

410 Contribution of carbonates is also significant in MSZ waters with proportions ranging from $0.71\%_{0.53}^{0.84}$ for S13 to $0.83\%_{0.69}^{0.92}$ for S15. Based on results of the mixing model, we are able to estimate a value for $\delta^{34}\text{S}$ of the pyrite endmember. Indeed, a significant linear negative relationship ($R^2 = 0.8$) exists between the $\delta^{34}\text{S}$ measured in springs across the Séchilienne massif and the modal estimates of their $X_{sil}^{SO_4}$. Intercept of this relationship, for $X_{sil}^{SO_4} = 1$ (equivalent to $X_{gyp}^{SO_4} = 0$) gives an estimate for $\delta^{34}\text{S}_{\text{sulfur}}$ of -3.5% . Such estimates are consistent with the range of measurements of solid sulfur reported in this study

415 (ranging between -13.1% to 17.8%) and should define an average value for the Séchilienne unstable zone.



420 Figure 5: Concentration in equivalents calculated for each endmember by the mixing model presented in the text and in Appendix (Table C2). Silicates contribute for Na+K+Ca+Mg (Na+K not indicated), carbonates for Ca+Mg, gypsum dissolution for Ca+Mg (not distinguished). Carbonic acid originates from soils. Sulfuric acid is generated by the oxidation of sulphide minerals in the fractured zone preferentially.

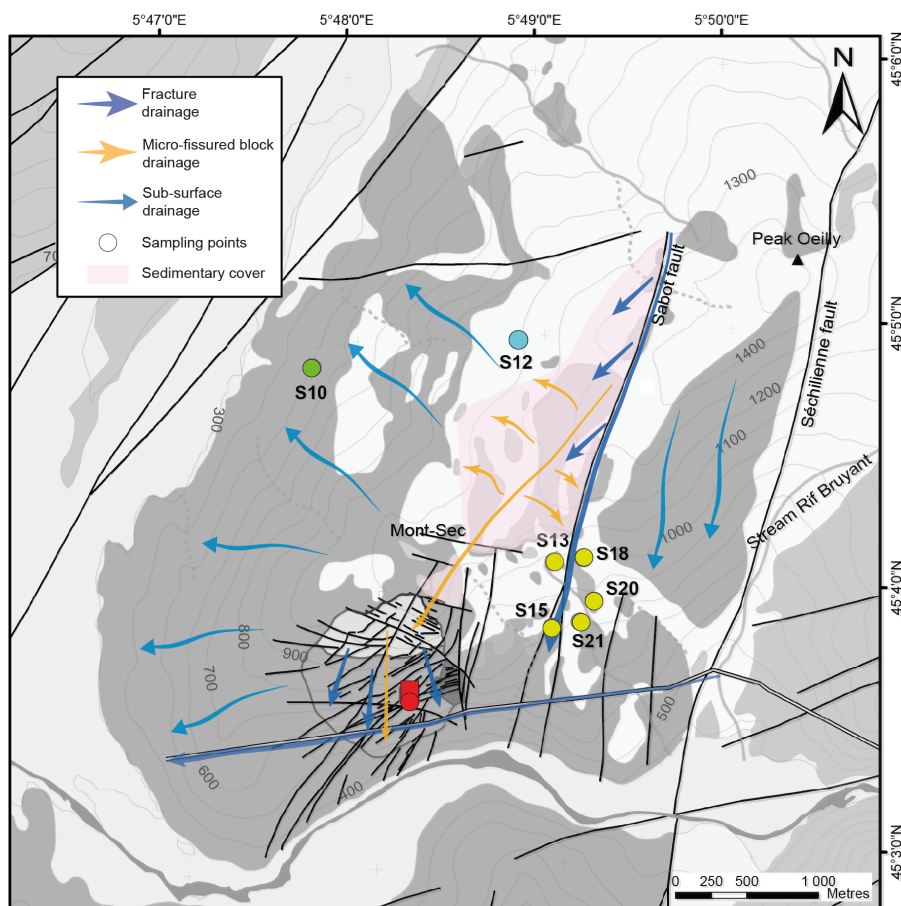
5.2 Implications for hydrogeological processes at the Séchilienne site

425 In unstable massifs contexts water plays important roles, first as being a hydrogeological process, aggravating factor of the massif. Secondly, water is a geochemical factor, which weather the massif, making it less cohesive. These two factors



interacting with each other in time and changing the permeability and consequently the water flowpaths through the massif. Hydrological triggering is the most usual mechanism of initiation and reactivation of landslides but water flows inside the system that involve the source and pathway of the waters have also been shown to have a major impact on the destabilization of a slope (de Montety et al. 2007; Guglielmi et al. 2002, Vallet et al. 2015b). The understanding of hydrogeological functioning of aquifers is thus essential to constrain hydrological triggering. However, landslides constitute very heterogeneous media due to their intense fracturation, which makes hydrogeological investigation complicated. The use of hydrochemistry and isotopic investigation is a good substitute to classical investigation since the groundwaters $^{87}\text{Sr}/^{86}\text{Sr}$ ratios have proved to be useful in determining the sources of solutes in natural waters (Négrel and deschamps, 1996, Négrel et al., 2001, Dotsika et al., 2010) and investigating mineral weathering reactions (Brass, 1975; Åberg et al., 1989; Bullen et al., 1996; Clow and Drever, 1996; Bullen and Kendall, 1998) and identifying mixing processes involving groundwaters of different sources (Woods et al., 2000; Frost and Toner, 2004; Singleton et al., 2006) also inside an unstable context (Deiana et al., 2018). In groundwaters, $\delta^{34}\text{S}$ values of dissolved SO_4^{2-} are used in aquifer studies to identify sulfate sources (Cortecci et al., 2002; Gammons et al., 2013; Moncaster et al., 2000). The Séchilienne hydrogeological model proposed by Vallet et al. (2015a) (Fig. 1c,d) was based on sulfates as a tracer of waters flowing through the instability with the assumption that all SO_4^{2-} measured in groundwaters are sourced from the pyrite oxidation. Based on sulfate, an hydraulic connection was established between the unstable zone and the MSZ waters (Fig. 1c). High sulfates concentrations in those waters were supposed to be derived from a mixture of 30% of waters from the UZ (drained through a micro-fissured matrix) and 70% from the sedimentary cover (drained through micro-fissured matrix and larger fractures).

Results from the present study partly support the hydrogeological model established by Vallet et al. (2015a) but allow us to identify the contribution of another –unexpected- end member corresponding to the dissolution of gypsum with a remote origin. Based on the geological map (Barfély et al. 1972) gypsum occurrences have been found remotely from the study zone and have been described upstream along the Sabot fault which lies at the North-East of the MSZ outflows. As the fault is a major flowpath (Lajaunie et al., 2019), draining aquifers hosted by the sedimentary cover to the MSZ outflows, it contributes to the enrichment in SO_4^{2-} of those waters (Fig. 6). Our study therefore indicates a significant evaporitic origin for the sulfates in the MSZ waters, challenging the interpretation of Vallet et al. (2015a) of a hydrogeological connection between waters of the unstable and stable zones. UZ and BSZ outflows exhibit a small contribution of evaporites to their sulfate's contents which can be explained by a contribution of waters flow through the Sabot faults toward the sedimentary cover and the basement formations (Fig. 6) Improving numerical and predictive models requires the incorporation of hydrological processes such as the dynamics of water circulation within a massif (directly dependent on fracturation, volumes of water involved, etc.). This study shows that isotopic proxies such as Sr and S isotopes ($^{87}\text{Sr}/^{86}\text{Sr}$, $\delta^{34}\text{S}$) coupled to water chemistry can be a very powerful tool to constrain groundwater origin and flowpaths in landslides and can substitute to tracer surveys, and are a good alternative for hydrogeological investigation in hard context such as unstable slopes.



460 Figure 6: Sketch of the groundwater conceptual model, modified after Vallet et al., (2015).

5.3 Role of landslides on silicate weathering and CO₂ consumption

Recent studies have shown the importance of pyrite oxidation, sulfuric acid production, and associated chemical weathering in active landslides (Emberson et al. 2015, Emberson et al. 2016). In the following paragraph we examine the potential
465 implications of the present study of the Séchillienne landslide for the global carbon cycle.

Rock weathering consumes atmospheric CO₂ and, associated to the precipitation of carbonates in the ocean, is the mechanism that has allowed for the sequestration of atmospheric CO₂ and consequently lower the Earth's surface temperature on geological timescales (Berner and Berner 2012). Rock forming-minerals uplifted to the Earth surface react with oxygen, carbonic acid produced by soil respiration, and sulfuric acid produced by the oxidation of sulfide minerals. The
470 following reactions describe how carbonic (equations 9 and 11) and sulfuric (equations 10 and 12) acids interact with schematic silicate (here wollastonite CaSiO₃) and carbonate minerals.



When Ca^{2+} reaches the ocean, over a time period longer than 0.1 to 1 Myr, the precipitation of $CaCO_3$ releases CO_2 into the ocean-atmosphere system according to the reaction:

480



The influence of the above reactions (equations 9-13) on atmospheric CO_2 partial pressure depends on the time scale considered (Torres et al., 2016). At short timescales (typically $< 10^5$ yrs), the chemistry of river discharge is able to influence the carbonate system in the ocean. Indeed, the delivery of alkalinity and Dissolved Inorganic Carbon (DIC) to the ocean to a ratio lower than that of the modern seawater ratio ($Alk/DIC \sim 1$) leads to increased dissolved CO_2 concentration, and consequently higher CO_2 content in the atmosphere through re-equilibration (Zeebe and Wolf-Gladrow, 2001). If the Alk/DIC ratio is higher than 1 but lower than 2, at time scales longer than that typical of carbonate precipitation in the ocean (10^5 to 10^6 yrs) but shorter than that of marine sulfate reduction to sulfide in sea bottom sediments (several 10^6 yrs), atmospheric CO_2 will increase because the precipitation of carbonates releases CO_2 to the ocean-atmosphere system that was not consumed on land by weathering reactions (combination of equations. 12 and 13) which should lead to global warming (Calmels et al., 2007). This mechanism has been invoked by Torres et al. (2014) for maintaining atmospheric CO_2 levels during the Himalayan orogeny, which otherwise should have led to a rapid atmospheric CO_2 depletion by enhanced silicate weathering. Finally, at timescales longer than that typical of sedimentary burial of sulfide in the ocean, only silicate weathering by carbonic acid leads to CO_2 sequestration (Berner et Berner, 1996; Calmels et al. 2007). Such a situation is obtained if the Alk/DIC ratio is higher than 2. Fig. 7 shows that all the waters produced in the Unstable Zone of Séchilienne fall into the regions where the impact of chemical weathering is a short-term or long-term CO_2 degassing, and thus an increase of CO_2 in the atmosphere. This is particularly true for the G1 and G2 waters. Equations 12 and 13 combined show that for one mole of sulfate produced and transported in by rivers to the ocean, one mole of CO_2 is degassed. Therefore, the CO_2 degassing ensuing delivery of UZ-type waters (G1 and G2) to the oceans will be 2-3 times higher than that resulting from the delivery of BSZ-type waters (S10). This key role of erosion processes, and in particular of landslides, as sources of CO_2 to the atmosphere lend support to the observations

Our study thus shows that the Séchilienne landslide is a hotspot of CO_2 release to the atmosphere. We suggest that chemical weathering in similar landslides throughout the Alps (i.e Clapière, Super Sauze and Valabres in French Alps, Rosone Italy) have a similar impact on global biogeochemical cycles and climate. Although it is beyond the scope of the present study to

505



quantify the CO₂ fluxes linked to weathering in the Séchilienne landslide - let alone to attempt an extrapolation of such local results to the scale of the Alpine range - our work clearly shows that silicate and carbonate weathering by sulfuric acid generated in landslide zones of active mountain ranges have a climatic impact. Furthermore, this impact contradicts the textbook view that silicate weathering in mountain ranges consumes CO₂ from the atmosphere and cool the global climate
510 (Raymo, 1991).

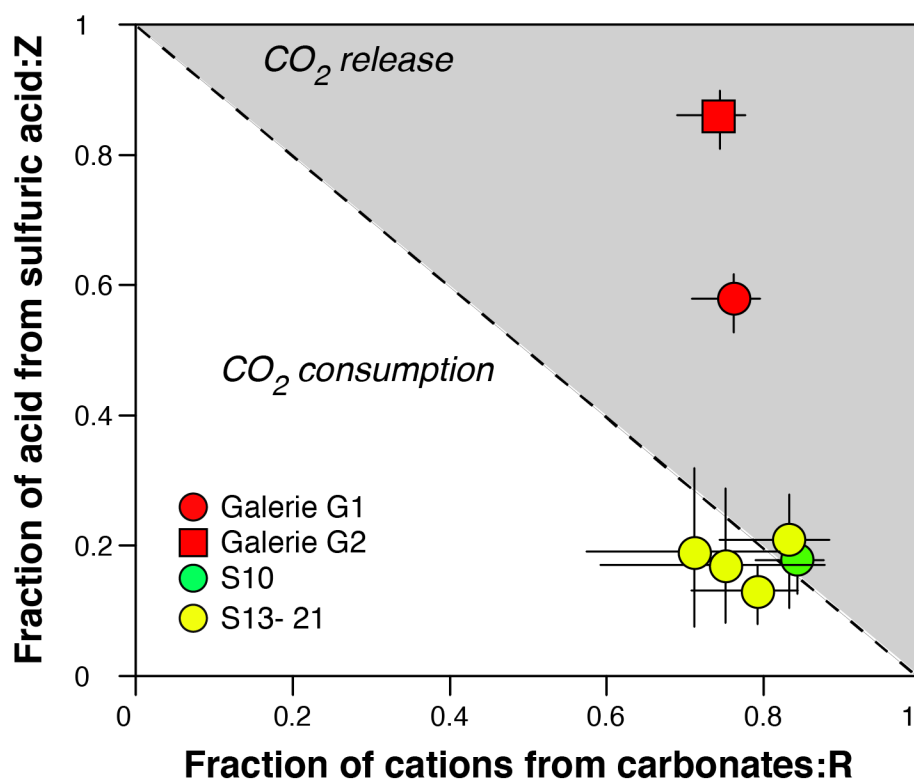


Figure 7: Diagram showing the Séchilienne landslide behaves as a long term CO₂ production to the atmosphere in its active part (adapted from Torres et al., 2016) because the cations are preferentially released in spring waters by the action of sulphuric acid and not carbonic acid from the soils (Table C3).
515

6. Conclusion

We use measurements of dissolved major element chemistry coupled to Sr and S isotopic ratios in waters draining at the Séchilienne landslide site in order to identify the chemical processes at play in the subsurface of the landslide area. Among
520 these tracers, strontium isotopes allow us to allocate cations to different sources, circumventing issues affecting elemental ratios related to the precipitation of secondary phases such as calcite. Silicate, carbonate, and evaporite weathering all appear



to contribute to the cation load of the Séchilienne waters. Sulfur isotopes bring a unique qualitative constraint on the origin of the sulfate ion, which is abundant in the Séchilienne groundwaters, showing the contribution of not only pyrite oxidation but also of gypsum dissolution.

525 The provenance of dissolved species at Séchilienne also reveals the complex water flow paths there. In particular, waters percolating through the landslide have acquired part of their chemical composition far away from the unstable zone itself. For example, sulfur isotopes clearly indicate an unexpected contribution from Triassic sedimentary gypsum dissolution, that can only occur in the sedimentary layers capping the upper part of the massif and pointing out the importance of water drainage by a major fault of the massif.

530 The comparison between the stable and unstable parts of the site shows that silicate weathering is enhanced in the fractured, unstable zone, where the landslide is active. Sulfur isotopes indicate that the production of acidity by the oxidation of magmatic sulfides enhances rock alteration in the unstable zone., This leads us to suggest the following feedback. By favoring the penetration of oxic waters and allowing contact with silicate minerals, fracturation and grain comminution controls the oxidation of pyrite that in turn rapidly generates sulfuric acid. The weathering of silicate minerals by sulfuric

535 acid weakens the rock structure what in turn favors fracturation in response to the gravitational stress. Fletcher et al. (2006) and recently Behrens et al. (2015) have shown that opening of porosity at the rock-soil interface in soil profiles can be initiated by oxidation of Fe(II) minerals inducing a positive volume budget leading to the production of micro-cracks, inducing further weathering, at the origin of the opening of fractures. At a larger scale, the feedback we propose here exemplifies a similar process of coupling between physical and chemical processes sustaining mass wasting in mountain

540 ranges.

Finally, we demonstrate that the Séchilienne landslide is a hotspot of CO₂ release to the atmosphere over the long term. Although it remains difficult to upscale the results of the present study to the entire Alpine range, or to a global scale, landslides developed on sulfide-hosting sedimentary rocks have a climatic impact opposite to the conventional view that rock weathering in mountains ranges consumes CO₂ from the atmosphere, and thus contributes to cool the global climate. In

545 addition, our study shows that strong control of weathering processes and rates by local hydrogeological features, such as the complexity of flow paths that determines the chemistry of the groundwaters within the unstable zone. More work is needed to assess the importance of landslides as hotspots of chemical alteration and geological CO₂ emissions, in particular to investigate their hydrological and hydrochemical response to weather and climate change. More generally, landslides epitomize the coupling between landscape evolution, tectonics and climate-weather. For this reason - and for their societal

550 impact in terms of natural hazard - monitoring landslides at over a range of time scales and frequency should become a priority.



Appendix B: Bedrock analyses

Table B1: Strontium isotopic compositions of rock samples of the Séchilienne slope

Sample	$^{86}\text{Sr}/^{87}\text{Sr}$	Sr (ppm)
Limestone (Lias)	0.7095	151.0
Limestone (Laffi)	0.7105	532.2
Vein (Calcite in)	0.7276	8.9
Micaschist	0.7350	59.3

565

Table B2: Sulfate isotopic compositions of bedrock samples of the Séchilienne slope

	Sample	Sampling dep	$\delta^{34}\text{S}$ (‰)	Mean $\delta^{34}\text{S}$	s.d
<i>Weathered micaschist</i>	SC2 19.71 A_1	19.71	-7.94	-0.74	9.36
	SC2 19.71 A_2	19.71	-7.76		
	SC2 19.71 B_1	17.71	-7.21		
	SC2 19.71 B_2	19.71	-7.01		
	SC2 108.50_1	108.5	17.77		
	SC2 108.50_2	108.5	17.56		
	SC2 132.50_1	132.5	1.67		
	SC2 132.50_2	132.5	1.99		
<i>Unweathered micaschist</i>	SC1 84.2 (1)_1	84.2	-6.58	-0.31	8.21
	SC1 84.2 (1)_2	84.2	-6.56		
	SC2 128_1	128	-4.12		
	SC2 128_2	128	-4.28		
	SC2 106.80_1	106.8	9.87		
	SC2 106.80_2	106.8	10.10		
	SC1 42.3 (5)_1	42.3	-3.32		
	SC1 42.3 (5)_2	42.3	-3.40		
	SC1 42.3 (5)_3	42.3	-3.21		
	SC1 80.3 (4)	80.3	0.88		
	SC1 30.60 (2)	30.6	-13.13		

Appendix C: Resolution of the geochemical mixing equations

570 Given the discussion of section 5.1 and the geochemical mixing diagrams presented in Figs. 4, three end members can be identified to release solutes to the springs of the Séchilienne area: silicate weathering (*sil*), carbonate weathering (*carb*), and gypsum dissolution (*gyp*). The contribution of each of these processes to the solute load of the springs can be estimated using a combination of mixing equations, provided that we can identify geochemical tracers that are conservative during mixing of compositionally different waters, and that the composition of the end members can be assessed. He we use two such tracers:

575 $^{87}\text{Sr}/^{86}\text{Sr}$ and Na/Sr ratios (all corrected from rain inputs, as explained in the main text). Indeed, the $^{87}\text{Sr}/^{86}\text{Sr}$ ratio is not



affected by isotope fractionation due to the way data are reduced after measurements by mass spectrometry; and both Na and Sr are soluble elements unlikely to be scavenged into secondary solids such as clays in most contexts. Two mixing equations, each based on one of the two tracers, can be combined with a third summation equation to solve for X_{sil}^{Sr} , X_{carb}^{Sr} , and X_{gyp}^{Sr} , the relative contribution of the three identified end member to dissolved Sr:

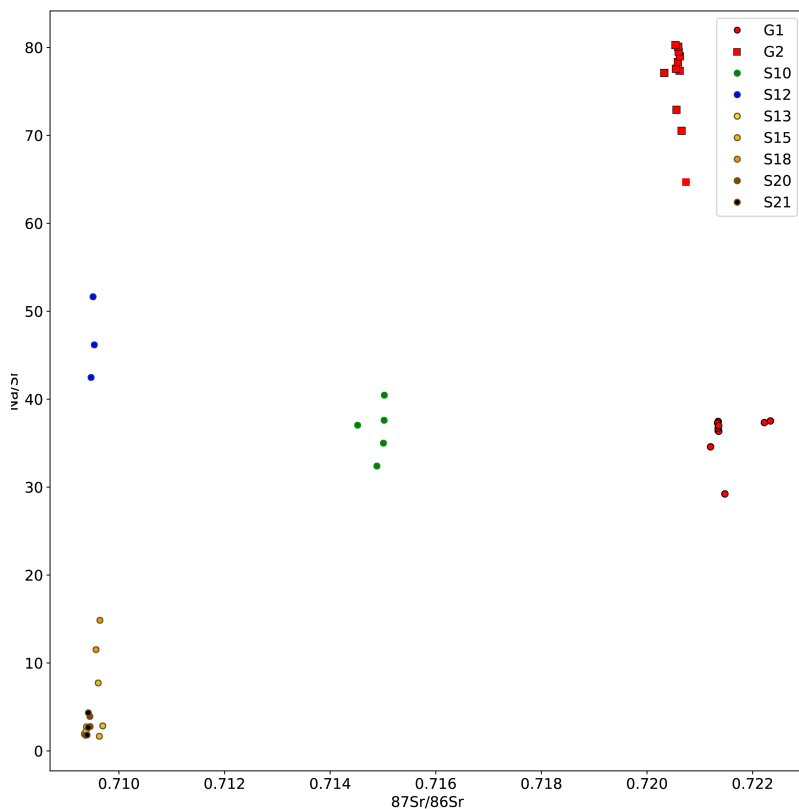
580

$$\left(\frac{^{87}Sr}{^{86}Sr}\right)_{spring} = X_{sil}^{Sr} \left(\frac{^{87}Sr}{^{86}Sr}\right)_{sil} + X_{carb}^{Sr} \left(\frac{^{87}Sr}{^{86}Sr}\right)_{carb} + X_{gyp}^{Sr} \left(\frac{^{87}Sr}{^{86}Sr}\right)_{gyp} \quad (C1)$$

$$\left(\frac{Na}{Sr}\right)_{spring} = X_{sil}^{Sr} \left(\frac{Na}{Sr}\right)_{sil} + X_{carb}^{Sr} \left(\frac{Na}{Sr}\right)_{carb} + X_{gyp}^{Sr} \left(\frac{Na}{Sr}\right)_{gyp} = X_{sil}^{Sr} \left(\frac{Na}{Sr}\right)_{sil} \quad (C2)$$

$$X_{sil}^{Sr} + X_{carb}^{Sr} + X_{gyp}^{Sr} = 1 \quad (C3)$$

585 The simplification of eq. (C2) is made possible by the fact that the gypsum and carbonate end members can be assumed to be devoid of Na. This assumption is supported by the positions of the different springs in a Na/Sr vs. $^{87}Sr/^{86}Sr$, which indicates that the low- $^{87}Sr/^{86}Sr$ component, encompassing both carbonate and gypsum weathering of the springs has a negligible Na content (Fig. C1).



590



Figure C1: Na/Sr vs $^{87}\text{Sr}/^{86}\text{Sr}$ in the different groups of water outflow from the Séchilienne massif.

The composition of the end members was constrained as follows (values also provided in Table A6):

- for each spring, $\left(\frac{^{87}\text{Sr}}{^{86}\text{Sr}}\right)_{spring}$ and $\left(\frac{\text{Na}}{\text{Sr}}\right)_{spring}$ were taken to be equal to the average ratios (corrected from rain inputs for Na/Sr) over all measurements available for the spring, with the corresponding standard deviation used as an estimate of the associated uncertainty (note that one outlier were dismissed for each of the two springs G1 and G2);
- $\left(\frac{^{87}\text{Sr}}{^{86}\text{Sr}}\right)_{carb}$ and $\left(\frac{^{87}\text{Sr}}{^{86}\text{Sr}}\right)_{gyp}$ were fixed at 0.7095 ± 0.0005 (representative of Jurassic seawater; MacArthur and Howarth, 2004) and 0.708 ± 0.001 (representative of Triassic seawater), respectively. These values also agree with those measured in the limestone bedrocks.
- $\left(\frac{^{87}\text{Sr}}{^{86}\text{Sr}}\right)_{sil}$ was assumed to be equal to the measured Sr isotope ratio for the local micaschist bedrock (0.735 ± 0.005).
- The $\left(\frac{\text{Na}}{\text{Sr}}\right)_{sil}$ ratio was determined for the springs the most affected by silicate weathering (G1, G2, and S10) by extrapolating Na/Sr vs. $^{87}\text{Sr}/^{86}\text{Sr}$ relationships (Fig. C1) to a $^{87}\text{Sr}/^{86}\text{Sr}$ equal to that of the silicate end member (0.735, see above). Linear extrapolation in this diagram is made possible by the fact that Sr concentration is present on the denominator of both ratios plotted. For each spring, a set of lines was determined, each passing through (1) the carbonate end member ($^{87}\text{Sr}/^{86}\text{Sr} = 0.7095$ and $\text{Na}/\text{Sr} = 0$); (2) one of the samples collected for this spring. After extrapolation of these lines to $^{87}\text{Sr}/^{86}\text{Sr} = 0.735$, a collection of estimated $\left(\frac{\text{Na}}{\text{Sr}}\right)_{sil}$ ratios was therefore obtained for each spring, and the average and standard deviation of these ratios was used as spring-specific central estimate and associated uncertainty of the $\left(\frac{\text{Na}}{\text{Sr}}\right)_{sil}$ ratio. The obtained values range from 76 ± 5 to 176 ± 11 , lower than those classically estimated for silicates (e.g. Négrel et al., 1993) but consistently with the fact that the micaschist at Séchilienne is a sedimentary rock that has lost soluble elements such as Na in previous weathering episodes compared to igneous silicates. For the springs the least affected by silicate weathering (S12, S13, S15, S18, S20, and S21), as such extrapolation would lack precision, we simply took the average and standard deviation of the $\left(\frac{\text{Na}}{\text{Sr}}\right)_{sil}$ ratios estimated for springs G1, G2, and S10 (yielding 142 ± 46). This strong assumption does not bear significant consequence on our overall evaluation as these former springs are not significantly affected by silicate weathering anyway.



The uncertainty on the different input parameters was propagated to the output variables (X_{sil}^{Sr} , X_{carb}^{Sr} , and X_{gyp}^{Sr}) using a Monte Carlo method based on 10,000 iterations. For this, at each of the 10,000 iterations a value for each input parameter (end member composition) was randomly picked following a normal distribution with mean equal and standard deviations to the estimate and uncertainty provided above, respectively. Runs yielding X_{sil}^{Sr} , X_{carb}^{Sr} , and X_{gyp}^{Sr} values outside of the range [0,1] were dismissed (the number of "valid" iterations is reported in Table C2). Note that the composition of the springs was not considered as a random variable here and was simply fixed for all iterations.

The resulting distributions of output values are reported in Table C2 as their 16th, 50th (median), and 84th percentile. Median estimates of X_{sil}^{Sr} range from 0.02 (springs S20 and S21) to 0.41 and 0.46 (springs G2 and G1, respectively); median estimates of X_{carb}^{Sr} range from 0.3 and 0.29 (springs S18 and G1) to 0.75 (spring S15); and median estimates of X_{gyp}^{Sr} are in the range 0.08-0.10 for all springs except S18 (0.48).

The contribution of each of these end members to the load of the dissolved major species SO_4 , Ca, and Mg is necessary to evaluate the impact of the different weathering processes to the CO_2 budget of the S echilienne area (Torres et al., 2016). This can be calculated from the contributions to dissolved Sr following:

$$X_i^E = X_i^{Sr} \left(\frac{E}{Sr} \right)_i / \left(\frac{E}{Sr} \right)_{spring} \quad (C4)$$

with $i = sil, carb, \text{ or } gyp$, and $E = SO_4, Mg, \text{ or } Ca$ (corrected from rain inputs). Therefore, to calculate these contributions, the $\left(\frac{E}{Sr} \right)_{spring}$ are necessary. We used the following assumptions:

- The E/Sr ratios of the gypsum end member were determined using the E/ SO_4 vs. (Ca+Mg)/ SO_4 relationships described by the springs the least affected by silicate weathering (as identified by their low $^{87}Sr/^{86}Sr$ ratios, *i.e.* springs S13, S15, S18, S20, and S21; Fig. C2). Indeed, for these springs were sulfate can be assumed to be derived only from gypsum and not from sulfide dissolution, when the (Ca+Mg)/ SO_4 is equal to 1, the entirety of the dissolved load can be assumed to be derived from gypsum dissolution alone (Ca and Mg being the two major cations likely to be released by gypsum dissolution). Linear extrapolation in this diagram is made possible by the fact that SO_4 concentration is present on the denominator of both ratios plotted. Taking the average values obtained through extrapolation of the observed trends to (Ca+Mg)/ $SO_4 = 1$ suggests 0.31 ± 0.04 , 0.69 ± 0.04 , and $9.2 \cdot 10^{-3} \pm 4.4 \cdot 10^{-3}$ for the Mg/ SO_4 , Ca/ SO_4 , and Sr/ SO_4 ratios of the gypsum end members. From these three SO_4 -normalized ratios, Sr-normalized ratios can be obtained to calculate X_{gyp}^E using eq. (C4).
- The SO_4/Sr ratio of the carbonate end member was assumed to be equal to 0, consistently with the mixing diagrams of Fig. 4.

650



Consequently, the SO₄/Sr ratio of the silicate end member could be estimated using the SO₄/Sr mixing equation (similar to eqs. (C1-C2)):

$$\left(\frac{SO_4}{Sr}\right)_{spring} = X_{sil}^{Sr} \left(\frac{SO_4}{Sr}\right)_{sil} + X_{gyp}^{Sr} \left(\frac{SO_4}{Sr}\right)_{gyp} \quad (C5)$$

655

to solve eq. (C5), the average and standard deviation of all measurements of $\left(\frac{SO_4}{Sr}\right)_{spring}$ were used, thereby yielding a spring-specific value for $\left(\frac{SO_4}{Sr}\right)_{sil}$. This estimate was performed during the Monte Carlo iterations described above, yielding modal values ranging from 734 (spring S10) to 1845 (spring G2).

660

- The Mg/Sr and Ca/Sr ratios of the silicate end member were taken in the range 150-200 following Négrel et al. (1993) and Gaillardet et al. (1999). Note that for the Monte Carlo iterations, these two parameters were assumed to follow a uniform distribution within this range, rather than a normal distribution as assumed for the other parameters.

665

As described for $\left(\frac{SO_4}{Sr}\right)_{sil}$ above, the Mg/Sr and Ca/Sr ratios of the carbonate end member were determined using the Mg/Sr and Ca/Sr mixing equations. These estimate were performed during the Monte Carlo iterations described above, yielding modal values ranging from 29 (spring S13) to 1117 (spring G1) for $\left(\frac{Mg}{Sr}\right)_{carb}$ and from 77 to 768 (same springs) for $\left(\frac{Ca}{Sr}\right)_{carb}$. These latter values are smaller than those expected from the dissolution of carbonates, which can be attributed to the precipitation of secondary carbonates which tend to favor Ca and leave the residual water with low Ca/Sr ratios (Bickle et al., 2015).

670

Doing so (Table C2), modal estimates of X_{sil}^{Mg} and X_{sil}^{Ca} range from 0.05 and 0.02 (spring S15) to 0.19 and 0.18 (spring G1), respectively. Modal estimates of X_{carb}^{Mg} and X_{carb}^{Ca} are in the range 0.40 and 0.54 (spring S15) to 0.84 and 0.78 (spring G1), respectively. Finally, X_{gyp}^{Mg} is lower than 0.10 for all springs, whereas modal estimates of X_{gyp}^{Ca} are in the range 0.12-0.21 for all springs except for springs G1, G2 and S10 (< 0.05).

675

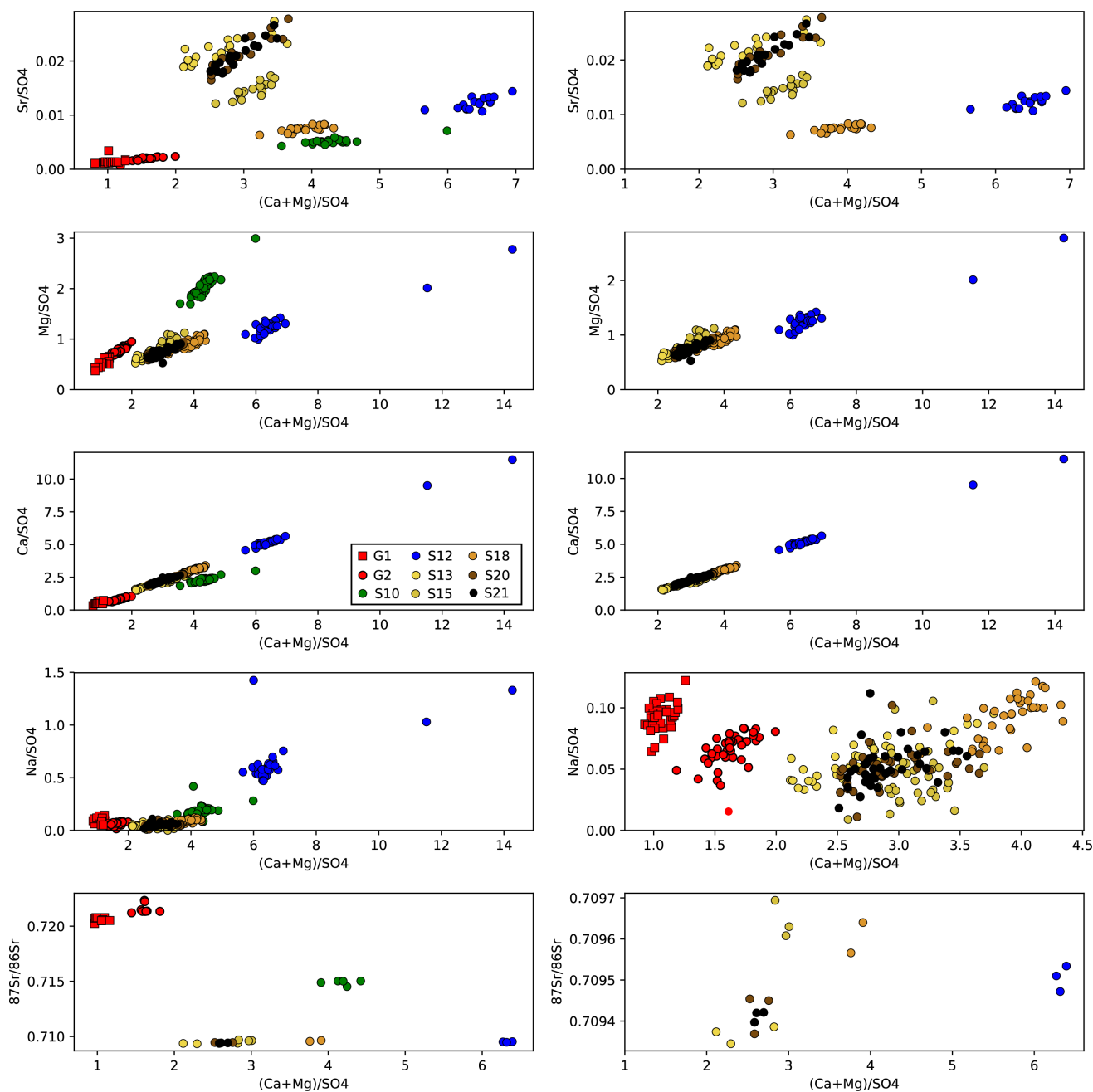
Modal estimates of $X_{sil}^{SO_4}$ are below 0.32 for springs S13-S21, and above 0.82 for springs G1, G2, and S10. Consequently, modal estimates of $X_{gyp}^{SO_4}$ range from 0.01 (springs G1 and G2) to 0.32 (S18).

680

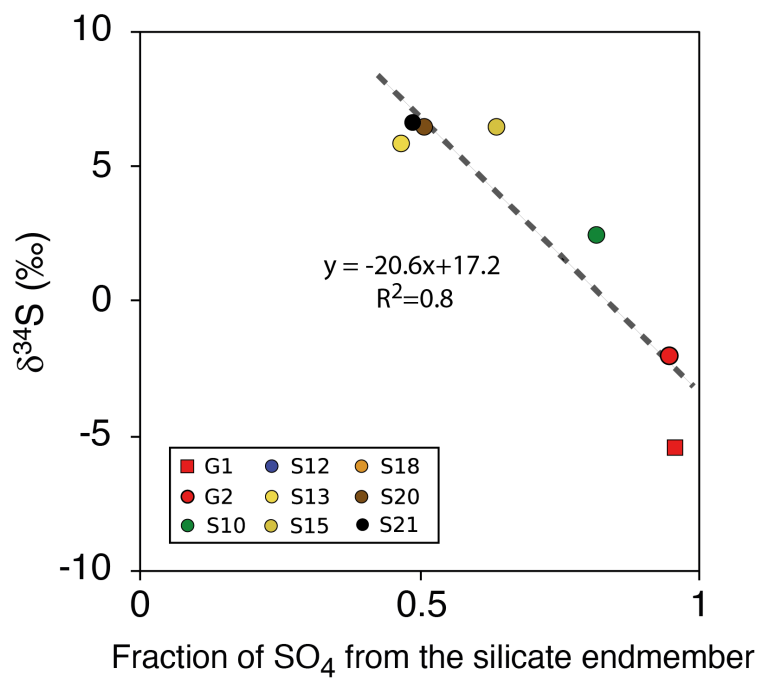
Finally, for each Monte Carlo iterations we calculated the "R" and "Z" parameters of Torres et al. (2016), representing the contribution of carbonate weathering to their total alkalinity, and the contribution of sulfuric acid to the acidity of the weathering reactions, respectively. Table C3 reports the results of these estimates, with modal estimates of R ranging from 0.63 (S13) to 0.85 (S10); and modal estimates of Z ranging from 0.13 (S18) to 0.86 (G2).



To assess the validity of our findings from the mixing model using independent measurements, our $\delta^{34}\text{S}$ measurements can be used. A significant linear negative relationship ($R^2 = 0.8$) exists between the $\delta^{34}\text{S}$ measured in springs across the S echilienne massif and the modal estimates of their $X_{sil}^{SO_4}$, consistent with the isotope composition of sulfur being driven by a binary mixture (Fig. C3). The intercept of this relationship ($X_{sil}^{SO_4} = 0$, equivalent to $X_{gyp}^{SO_4} = 1$) yields an estimate for $\delta^{34}\text{S}_{gyp} =$
685 17.2‰, while extrapolation to $X_{sil}^{SO_4} = 1$ indicates $\delta^{34}\text{S}_{sulfur} = -3.5$ ‰. Such estimates are fully consistent with our own measurements of solid sulfur at S echilienne, as well as with reported measurements for Triassic seawater where local gypsum might have formed.



690 Figure C2: Mixing diagrams of E/SO_4 vs. $(Ca+Mg)/SO_4$ (with $E = Sr, Mg, Ca, Na$ and $^{87}Sr/^{86}Sr$) used to determine the E/Sr ratios of the gypsum end member.



695 Figure C3: $\delta^{34}\text{S}$ measured in springs across the S echilienne massif vs modal estimates of their fraction of SO_4 from silicate endmember:
 $X_{sil}^{\text{SO}_4}$

700

705

Table C1: Inputs of the mixing model with silicate, carbonate and gypsum endmembers



Outflow	Spring average composition				Carbonate end member		
	$^{87}\text{Sr}/^{86}\text{Sr}$	SO4/Sr	Mg/Sr	Ca/Sr	Na/Sr	$^{87}\text{Sr}/^{86}\text{Sr}$	
						Mean	s.d.
G1	0.7215	571	418	444	34	0.7095	0.0005
G2	0.7205	785	397	410	70	0.7095	0.0005
S10	0.7148	195	399	437	37	0.7095	0.0005
S12	0.7095	82	103	425	48	0.7095	0.0005
S13	0.7093	46	32	89	2.6	0.7095	0.0005
S15	0.7096	69	63	150	2.5	0.7095	0.0005
S18	0.7096	134	126	397	12	0.7095	0.0005
S20	0.7094	48	35	103	2	0.7095	0.0005
S21	0.7094	48	35	103	2.4	0.7095	0.0005

Outflow	Silicate end member							
	$^{87}\text{Sr}/^{86}\text{Sr}$		Mg/Sr		Ca/Sr		Na/Sr	
	Mean	s.d.	Low	High	Low	High	Mean	s.d.
G1	0.735	0.005	150	200	150	200	76	5
G2	0.735	0.005	150	200	150	200	176	11
S10	0.735	0.005	150	200	150	200	172	13
S12	0.735	0.005	150	200	150	200	141	46
S13	0.735	0.005	150	200	150	200	141	40.
S15	0.735	0.005	150	200	150	200	141	35
S18	0.735	0.005	150	200	150	200	141	32
S20	0.735	0.005	150	200	150	200	141	30
S21	0.735	0.005	150	200	150	200	141	28

Outflow	Gypsum end member							
	$^{87}\text{Sr}/^{86}\text{Sr}$		Sr/SO4		Mg/SO4		Ca/SO4	
	Mean	s.d.	Mean	s.d.	Mean	s.d.	Mean	s.d.
G1	0.708	0.001	0.009	0.004	0.310	0.041	0.689	0.041
G2	0.708	0.001	0.009	0.004	0.310	0.041	0.689	0.041
S10	0.708	0.001	0.009	0.004	0.310	0.041	0.689	0.041
S12	0.708	0.001	0.009	0.004	0.310	0.041	0.689	0.041
S13	0.708	0.001	0.009	0.004	0.310	0.041	0.689	0.041
S15	0.708	0.001	0.009	0.004	0.310	0.041	0.689	0.041
S18	0.708	0.001	0.009	0.004	0.310	0.041	0.689	0.041
S20	0.708	0.001	0.009	0.004	0.310	0.041	0.689	0.041
S21	0.708	0.001	0.009	0.004	0.310	0.041	0.689	0.041

710

Table C2: Results of mixing calculations

Outflow	Fractions Sr			Fractions Mg			Fractions Ca			Fractions SO4		Fractions total cationic charge			number of valid iterations
	$X_{\text{Sr}}^{\text{sil,carb,gyp}}$			$X_{\text{Mg}}^{\text{sil,carb,gyp}}$			$X_{\text{Ca}}^{\text{sil,carb,gyp}}$			$X_{\text{SO4}}^{\text{sil,gyp}}$					
	Silicate	Carbonate	Gypsum	Silicate	Carbonate	Gypsum	Silicate	Carbonate	Gypsum	Silicate	Gypsum	Silicate	Carbonate	Gypsum	
G1	0.46 \pm 0.04	0.29 \pm 0.04	0.25 \pm 0.03	0.19 \pm 0.04	0.78 \pm 0.04	0.02 \pm 0.03	0.18 \pm 0.04	0.78 \pm 0.04	0.04 \pm 0.03	0.95 \pm 0.04	0.05 \pm 0.03	0.21 \pm 0.04	0.76 \pm 0.04	0.03 \pm 0.03	1143
G2	0.41 \pm 0.04	0.32 \pm 0.04	0.27 \pm 0.03	0.18 \pm 0.04	0.80 \pm 0.04	0.02 \pm 0.03	0.17 \pm 0.04	0.78 \pm 0.04	0.05 \pm 0.03	0.96 \pm 0.04	0.04 \pm 0.03	0.22 \pm 0.04	0.74 \pm 0.04	0.04 \pm 0.03	1288
S10	0.22 \pm 0.03	0.46 \pm 0.04	0.32 \pm 0.03	0.10 \pm 0.03	0.88 \pm 0.04	0.03 \pm 0.03	0.09 \pm 0.03	0.86 \pm 0.04	0.06 \pm 0.03	0.82 \pm 0.03	0.18 \pm 0.03	0.11 \pm 0.03	0.84 \pm 0.03	0.04 \pm 0.03	2973
S13	0.02 \pm 0.02	0.73 \pm 0.03	0.25 \pm 0.04	0.10 \pm 0.03	0.65 \pm 0.03	0.25 \pm 0.04	0.03 \pm 0.02	0.76 \pm 0.03	0.20 \pm 0.04	0.49 \pm 0.04	0.51 \pm 0.03	0.06 \pm 0.03	0.71 \pm 0.03	0.23 \pm 0.04	3234
S15	0.02 \pm 0.02	0.75 \pm 0.03	0.23 \pm 0.03	0.05 \pm 0.02	0.83 \pm 0.03	0.12 \pm 0.03	0.02 \pm 0.02	0.86 \pm 0.03	0.12 \pm 0.03	0.65 \pm 0.03	0.35 \pm 0.04	0.04 \pm 0.03	0.83 \pm 0.03	0.13 \pm 0.03	5039
S18	0.08 \pm 0.02	0.24 \pm 0.03	0.68 \pm 0.03	0.11 \pm 0.03	0.72 \pm 0.03	0.17 \pm 0.03	0.03 \pm 0.02	0.84 \pm 0.03	0.12 \pm 0.03	0.51 \pm 0.03	0.49 \pm 0.03	0.06 \pm 0.03	0.79 \pm 0.03	0.14 \pm 0.03	1667
S20	0.02 \pm 0.02	0.74 \pm 0.03	0.24 \pm 0.03	0.08 \pm 0.02	0.69 \pm 0.03	0.22 \pm 0.03	0.03 \pm 0.02	0.80 \pm 0.03	0.17 \pm 0.03	0.51 \pm 0.03	0.49 \pm 0.03	0.05 \pm 0.02	0.75 \pm 0.03	0.20 \pm 0.03	3885
S21	0.02 \pm 0.02	0.74 \pm 0.03	0.24 \pm 0.03	0.08 \pm 0.02	0.69 \pm 0.03	0.22 \pm 0.03	0.03 \pm 0.02	0.80 \pm 0.03	0.17 \pm 0.03	0.50 \pm 0.03	0.50 \pm 0.03	0.05 \pm 0.02	0.75 \pm 0.03	0.20 \pm 0.03	3822

footnote: proportions are reported as the median value (50%) \pm s.d

715



Table C3: R & Z parameters calculations, following Torres et al. 2016

Outflow	Parameters as in Torres et al. (2016)		Number of valid iterations	$\delta^{34}\text{S}$		
	R	Z		Sample	Silicate (sulfur)	Gypsum
G1	$0.75_{0.07}^{0.79}$	$0.58_{0.04}^{0.64}$	1143	-2.12	17.59	-3.48
G2	$0.74_{0.07}^{0.79}$	$0.86_{0.08}^{0.88}$	1288	-5.45	17.59	-3.48
S10	$0.84_{0.07}^{0.87}$	$0.18_{0.02}^{0.21}$	2973	2.38	17.59	-3.48
S13	$0.71_{0.05}^{0.82}$	$0.19_{0.02}^{0.29}$	3234	5.78	17.59	-3.48
S15	$0.83_{0.07}^{0.92}$	$0.21_{0.02}^{0.28}$	5039	6.39	17.59	-3.48
S18	$0.79_{0.07}^{0.84}$	$0.13_{0.01}^{0.17}$	1667		17.59	-3.48
S20	$0.75_{0.07}^{0.87}$	$0.17_{0.02}^{0.24}$	3885	6.38	17.59	-3.48
S21	$0.75_{0.07}^{0.87}$	$0.17_{0.02}^{0.24}$	3822	6.54	17.59	-3.48

footnote: proportions are reported as the median value (50%) \pm s.d

720 Team list

Pierre Nevers

Julien Bouchez

Jérôme Gaillardet

Thomazo Christophe

725 Laetia Faure

Catherine Bertrand

Author contribution

730 Pierre Nevers measured the Sr isotopic ratios, worked on the interpretation and wrote the paper. Julien Bouchez and Jérôme Gaillardet helped in the isotopic measurements, in the inversion calculations and in writing the paper. Christophe Thomazo measured the sulfur isotopic ratios. Laetia Faure helped with the Sr isotope measurements. Catherine Bertrand organized the sampling strategy and is in charge of the Séchilienne Observatory.

Competing interests

The authors declare that they have no conflict of interest.



735 Acknowledgments

Part of this work was supported by IPGP multidisciplinary program PARI and by Region île-de-France SESAME Grant no. 12015908. Caroline Gorge is acknowledged for her analytical work.

References

740 Barféty, J., Bordet, P., Carme, F., Debelmas, J., Meloux, M., Montjuvent, G., Sarrot Reynauld, J.: Carte géologique détaillée de la France (1/50000) n°797 Vizille. Editions du BRGM, p. 38, 1972

Baudement, C., Bertrand, C., Guglielmi, Y., Viseur, S., Vallet, A., & Cappa, F.: Quantification de la dégradation mécanique et chimique d'un versant instable : approche géologique, hydromécanique et hydrochimique Etude du versant instable de Séchilienne, Isère (38). 1–6, 2013

745

Berner, K.E. and Berner, R.A.: Global Environment: Water, Air and Geochemical Cycles, Princeton Univ. Press, 369–382, 2012

750 Bertrand, C., Vallet, A., Mudry, J.: Hydrochemical Approach of Mechanical Degradation of the Séchilienne Unstable Slope, in Engineering Geology for Society and Territory – Volume 2, edited by: Lollino, G., Giordan, Crosta, G. B., Corominas, J., Azzam, R., Wasowski, J., Sciarra, N., Springer International Publishing Switzerland, chapter: 383, https://doi.org/10.1007/978-3-319-09057-3_383, 2015

755 Bickle, M. J., Tipper, E. T., Galy, A., Chapman, H., and Harris, N.: On Discrimination Between Carbonate and Silicate Inputs to Himalayan Rivers, *Am. J. Sci.*, 315, 120–166, <https://doi.org/10.2475/02.2015.02>, 2015

Binet, S., Spadini, L., Bertrand, C., Guglielmi, Y., Mudry, J., and Scavia, C.: Variability of the groundwater sulfate concentration in fractured rock slopes: a tool to identify active unstable areas, *Hydrol. Earth Syst. Sci.*, 13, 2315–2327, <https://doi.org/10.5194/hess-13-2315-2009>, 2009

760

Blattmann T. M., Wang, S. L., Lupker, M., Märki, L., Haghypour, N., Wacker, L., Chung, L. H., Bernasconi, S. M., Plötze, M., Eglinton, T. I.: Sulphuric acid-mediated weathering on Taiwan buffers geological atmospheric carbon sinks, *Sci Rep.*, 2945, <https://doi.org/10.1038/s41598-019-39272-5>, 2019

765 Brass, G. W.: The effect of weathering on the distribution of strontium isotopes in weathering profiles. *Geochimica et Cosmochimica Acta*, 39, 1647–1653, [https://doi.org/10.1016/0016-7037\(75\)90086-1](https://doi.org/10.1016/0016-7037(75)90086-1), 1975



- 770 Bullen, T. D., Krabbenhoft, D. P., Kendall, C.: Kinetic and mineralogic controls on the evolution of groundwater chemistry and $^{87}\text{Sr}/^{86}\text{Sr}$ in a sandy silicate aquifer, northern Wisconsin, USA. *Geochimica et Cosmochimica Acta*, 60(10), 1807–1821, [https://doi.org/10.1016/0016-7037\(96\)00052-X](https://doi.org/10.1016/0016-7037(96)00052-X), 1996
- 775 Burke, W.H., Denison, R.E., Hetherington, E.A., Koepnick, R.B., Nelson, H.F. and Otto, J.B.: Variation of seawater $^{87}\text{Sr}/^{86}\text{Sr}$ throughout Phanerozoic time. *Geology* 10: 516-519., [https://doi.org/10.1130/0091-7613\(1982\)10<516:VOSSTP>2.0.CO;2](https://doi.org/10.1130/0091-7613(1982)10<516:VOSSTP>2.0.CO;2), 1982
- 780 Calmels, D., Gaillardet, J., Brenot, A., & France-Lanord, C.: Sustained sulfide oxidation by physical erosion processes in the Mackenzie River basin: Climatic perspectives, *Geology*, 35(11), 1003–1006, <https://doi.org/10.1130/G24132A.1>, 2007
- 785 Canfield, D. E., Raiswell, R., Westrich, J. T., Reaves, C. M., Berner, R. A.: the use of chromium reduction in the analysis of reduced inorganic sulfur in sediments and shales, *Chemical Geology*, 54(1-2), 149–155, [https://doi.org/10.1016/0009-2541\(86\)90078-1](https://doi.org/10.1016/0009-2541(86)90078-1), 1986
- 790 Cappa, F., Guglielmi, Y., Soukatchoff, V., Mudry, J., Bertrand, C., Charmoille, A.: Hydromechanical modeling of a large moving rock slope inferred from slope levelling coupled to spring long-term hydrochemical monitoring: example of the La Clapière landslide (Southern Alps, France), *Journal of Hydrology*, 291(1–2), 67–90, <https://doi.org/10.1016/J.JHYDROL.2003.12.013>, 2004
- 795 Cervi, F., Ronchetti, F., Martinelli, G., Bogaard, T. A., and Corsini, A.: Origin and assessment of deep groundwater inflow in the Ca' Lita landslide using hydrochemistry and in situ monitoring, *Hydrol. Earth Syst. Sci.*, 16, 4205–4221, <https://doi.org/10.5194/hess-16-4205-2012>, 2012
- 800 Clow, D. W and Drever, J. I.: Weathering rates as a function of flow through an alpine soil, *Chemical Geology*, 132(1–4), 131–141, [https://doi.org/10.1016/S0009-2541\(96\)00048-4](https://doi.org/10.1016/S0009-2541(96)00048-4), 1996
- Cortecci, G., Dinelli, E., Bencini, A., Adorni-Braccesi, A., La Ruffa, G.: Natural and anthropogenic SO_4 sources in the Arno river catchment, northern Tuscany, Italy: a chemical and isotopic reconnaissance, *Applied Geochemistry*, 17(2), 79–92, [https://doi.org/10.1016/S0883-2927\(01\)00100-7](https://doi.org/10.1016/S0883-2927(01)00100-7), 2002



- 805 Deiana, M., Cervi, F., Pennisi, M., Mussi, M., Bertrand, C., Tazioli, A., Ronchetti, F.: Chemical and isotopic investigations ($\delta^{18}\text{O}$, $\delta^2\text{H}$, 3H , $87\text{Sr}/86\text{Sr}$) to define groundwater processes occurring in a deep-seated landslide in flysch. *Hydrogeology Journal*, 26(8), 2669–2691, <https://doi.org/10.1007/s10040-018-1807-1>, 2018
- Dotsika, E., Poutoukis, D., Kloppmann, W., Guerrot, C., Voutsas, D., Kouimtzis, T. H.: The use of O, H, B, Sr and S isotopes for tracing the origin of dissolved boron in groundwater in Central Macedonia, Greece. *Applied Geochemistry*, 25(11), 1783–1796. <https://doi.org/10.1016/J.APGEOCHEM.2010.09.006>, 2010
- 810 Dubois, L., Chanut, M.-A., Duranthon, J. P.: Amélioration continue des dispositifs d’auscultation et de surveillance intégrés dans le suivi du versant instable des Ruines de Séchilienne in : *Géologues*, 182, edited by : Editions du BRGM, 50–55, 2014
- Emberson, R., Hovius, N., Galy, A. Marc, O.: Chemical weathering in active mountain belts controlled by stochastic bedrock landsliding, *Nature Geoscience*, 9, 42–45, <https://doi.org/10.1038/ngeo2600>, 2015
- 815 Emberson, R., Hovius, N., Galy, A., Marc, O.: Oxidation of sulfides and rapid weathering in recent landslides, *Earth Surface Dynamics*, 4(3), 727–742, <https://doi.org/10.5194/esurf-4-727-2016>, 2016b
- Emberson, R., Galy, A., Hovius, N.: Weathering of Reactive Mineral Phases in Landslides Acts as a Source of Carbon Dioxide in Mountain Belts, *Journal of Geophysical Research: Earth Surface*, 123(10), 2695–2713. <https://doi.org/10.1029/2018JF004672>, 2018
- 820 Fanlo, I. and Ayora, C.: The evolution of the Lorraine evaporitic basin: implications for the chemical and isotope composition of the Triassic ocean, *Chemical Geology*, vol. 146 n° 3-4, p. 135–154, [https://doi.org/10.1016/S0009-2541\(98\)00007-2](https://doi.org/10.1016/S0009-2541(98)00007-2), 1998
- 825 Frost, C. D., Toner, R. N.: Strontium isotopic identification of water-rock interaction and ground water mixing, *Ground Water*, 42(3), 418–432, <https://doi.org/10.1111/j.1745-6584.2004.tb02689.x>, 2004
- 830 Gaillardet, J., Dupre, B., Allegre C. J., Négrel, P.: Chemical and physical denudation in the Amazon River Basin, *Chemical Geology*, vol. 142 n° 3–4, p. 141–173, [https://doi.org/10.1016/S0009-2541\(97\)00074-0](https://doi.org/10.1016/S0009-2541(97)00074-0), 1997
- Gaillardet, J., Dupre, B., Louvat, P., Allegre, C. J.: Global silicate weathering and CO₂ consumption rates deduced from the chemistry of large rivers, *Chemical Geology*, 159, 3–30, [https://doi.org/10.1016/S0009-2541\(99\)00031-5](https://doi.org/10.1016/S0009-2541(99)00031-5), 1999



835

Gammons, C. H., Brown, A., Poulson, S. R., Henderson, T. H.: Using stable isotopes (S, O) of sulfate to track local contamination of the Madison karst aquifer, Montana, from abandoned coal mine drainage, *Applied Geochemistry*, 31, 228–238, <https://doi.org/10.1016/J.APGEOCHEM.2013.01.008>, 2013

840

Guglielmi, Y., Vengeon, J., Bertrand, C., Mudry, J., Follacci, J., Giraud, A.: Hydrogeochemistry: an investigation tool to evaluate infiltration into large moving rock masses (case study of La Clapière and Séchilienne alpine landslides), *Bulletin of Engineering Geology and the Environment*, 61(4), 311–324. <https://doi.org/10.1007/s10064-001-0144-z>, 2002

845

Hajj, F., Poszwa, A., Bouchez, J., Guérol, F.: Radiogenic and “stable” strontium isotopes in provenance studies: A review and first results on archaeological wood from shipwrecks, *Journal of Archaeological Science*, 86, 24–49, <https://doi.org/10.1016/j.jas.2017.09.005>, 2017

850

Kampschulte, A., Strauss, H.: The sulfur isotopic evolution of Phanerozoic seawater based on the analysis of structurally substituted sulfate in carbonates, *Chemical Geology*, 204(3–4), 255–286, <https://doi.org/10.1016/j.chemgeo.2003.11.013>, 2004

855

Koepnick, R. B., Denison, R. E., Burke, W. H., Hetherington, E. A., Dahl, D. A.: Construction of the Triassic and Jurassic portion of the Phanerozoic curve of seawater $^{87}\text{Sr}/^{86}\text{Sr}$, *Chemical Geology: Isotope Geoscience Section*, 80(4), 327–349, [https://doi.org/10.1016/0168-9622\(90\)90014-4](https://doi.org/10.1016/0168-9622(90)90014-4), 1990

860

Lajaunie, M., Gance, J., Nevers, P., Malet, J.-P., Bertrand, C., Garin, T., and Ferhat, G.: Structure of the Séchilienne unstable slope from large-scale 3d electrical tomography using a resistivity distributed automated system (r-das). *Geophysical Journal International*, <https://doi.org/10.1093/gji/ggz259>, 2019

865

Lasaga, A. C.: Chemical kinetics of water-rock interactions, *Journal of Geophysical Research: Solid Earth*, 89(B6), 4009–4025, <https://doi.org/10.1029/jb089ib06p04009>, 1984

865

Lerman, A., Wu, L., Mackenzie, F. T.: CO₂ and H₂SO₄ consumption in weathering and material transport to the ocean, and their role in the global carbon balance, *Marine Chemistry*, 106(1-2 SPEC. ISS.), 326–350, <https://doi.org/10.1016/j.marchem.2006.04.004>, 2007



- Le Roux, O., Jongmans, D., Kasperski, J., Schwartz, S., Potherat, P., Lebrouc, V., Meric, O.: Deep geophysical investigation of the large Séchilienne landslide (Western Alps, France) and calibration with geological data, *Engineering Geology*, 120(1–4), 18–3, <https://doi.org/10.1016/J.ENGGEOL.2011.03.004>, 2011
- 870
- Li, S. L., Calmels, D., Hana, G., Gaillardet, J., Liu, C. Q.: Sulfuric acid as an agent of carbonate weathering constrained by $\delta^{13}\text{CDIC}$: Examples from Southwest China, *Earth and Planetary Science Letters*, 270, 3–4, 30, 189–199, <https://doi.org/10.1016/j.epsl.2008.02.039>, 2008
- 875
- Maréchal, J.-C., 1998. Les circulations d'eau dans les massifs cristallins alpins et leurs relations avec les ouvrages souterrains, Ecole Polytechnique Fédérale de Lausanne (EPFL), 1998
- Merici, O., Garambois, S., Jongmans, D., Wathelet, M., Chatelain, J. L., Vengeon, J. M.: Application of geophysical methods for the investigation of the large gravitational mass movement of Séchilienne, France, *Canadian Geotechnical Journal*, 42(4), 880 1105–1115, <https://doi.org/10.1139/t05-034>, 2005
- Meybeck Michel. Composition chimique des ruisseaux non pollués en France. Chemical composition of headwater streams in France. In: *Sciences Géologiques*, tome 39, n°1, pp. 3–77, <https://doi.org/10.3406/sgeol.1986.1719>, 1986
- 885
- Meynadier, L., Gorge, C., Birck, J., Allègre, C.: Automated separation of Sr from natural water samples or carbonate rocks by high performance ion chromatography, *Chemical Geology*, 227(1–2), <https://doi.org/10.1016/j.chemgeo.2005.05.012>, 2006
- Moncaster, S. J., Bottrell, S. H., Tellam, J. H., Lloyd, J. W., Konhauser, K. O.: Migration and attenuation of agrochemical 890 pollutants: Insights from isotopic analysis of groundwater sulphate, *Journal of Contaminant Hydrology*, 43(2), 147–163, [https://doi.org/10.1016/S0169-7722\(99\)00104-7](https://doi.org/10.1016/S0169-7722(99)00104-7), 2000
- Montety, V. de, Marc, V., Emblanch, C., Malet, J.-P., Bertrand, C., Maquaire, O., Bogaard, T. A.: Identifying the origin of 895 groundwater and flow processes in complex landslides affecting black marls: insights from a hydrochemical survey, *Earth Surface Processes and Landforms*, 32(1), 32–48, <https://doi.org/10.1002/esp.1370>, 2007
- Montjuvent, G. and Winistorfer, J.: Glaciations quaternaires dans les Alpes franco-suissees et leur piedmont, in *Géologie Alpine*, 56, 251–282, 1980



- 900 Mudry, J., & Etievant, K., 2007. Synthèse hydrogéologique du versant instable des Ruines de Séchilienne (Unpublished report), UMR Chrono-Environnement, University of Franche-Comté, Besançon, 2007
- Négrel, P., Allègre, C. J., Dupré, B., Lewin, E.: Erosion sources determined by inversion of major and trace element ratios and strontium isotopic ratios in river: The Congo Basin case, *Earth and Planetary Science Letters*, 120(1–2), 59–76,
905 [https://doi.org/10.1016/0012-821X\(93\)90023-3](https://doi.org/10.1016/0012-821X(93)90023-3), 1993
- Négrel, P. and Deschamps, P.: Natural and anthropogenic budgets of a small watershed in the massif central (France): Chemical and strontium isotopic characterization of water and sediments, *Aquatic Geochemistry*, 2(1), 1–27,
<https://doi.org/10.1007/BF00240851>, 1996
- 910
- Négrel, P., Casanova, J., Aranyosy, J.-F.: Strontium isotope systematics used to decipher the origin of groundwaters sampled from granitoids: the Vienne Case (France), *Chemical Geology*, 177(3–4), 287–308, [https://doi.org/10.1016/S0009-2541\(00\)00414-9](https://doi.org/10.1016/S0009-2541(00)00414-9), 2001
- 915 Oudin, L., Hervieu, F., Michel, C., Perrin, C., Andréassian, V., Anctil, F., and Loumagne, C.: Which potential evapotranspiration input for a lumped rainfall–runoff model?: Part 2—towards a simple and efficient potential evapotranspiration model for rainfall–runoff modelling, *Journal of hydrology*, 303(1–4):290–306, 2005
- Raymo, M. E.: Geochemical evidence supporting T. C. Chamberlin's theory of glaciation, *Geology*, 19, 344–347,
920 [https://doi.org/10.1130/0091-7613\(1991\)019<0344:GESTCC>2.3.CO;2](https://doi.org/10.1130/0091-7613(1991)019<0344:GESTCC>2.3.CO;2), 1991
- Raymo, M., Ruddiman, W.: Tectonic forcing of late Cenozoic climate, *Nature*, 359, 117–122,
<https://doi.org/10.1038/359117a0>, 1992
- 925 Russell, W. A. and Papanastassiou, D. A.: Calcium isotope fractionation in ion-exchange chromatography, *Analytical Chemistry*, 50(8), 1151–1154, <https://doi.org/10.1021/ac50030a036>, 1978
- Singleton, M. J., Maher, K., DePaolo, D. J., Conrad, M. E., Evan Dresel, P.: Dissolution rates and vadose zone drainage from strontium isotope measurements of groundwater in the Pasco Basin, WA unconfined aquifer, *Journal of Hydrology*,
930 321(1–4), 39–58, <https://doi.org/10.1016/J.JHYDROL.2005.07.044>, 2006



- Spence, J., Telmer, K.: The role of sulfur in chemical weathering and atmospheric CO₂ fluxes: evidence from major ions, $\delta^{13}\text{C}_{\text{DIC}}$, and $\delta^{34}\text{S}$ SO₄ in rivers of the Canadian Cordillera, *Geochimica Cosmochimica*, 69, 5441–5458, <https://doi.org/10.1016/j.gca.2005.07.011>, 2005
- 935
- Stallard, R. F. and Edmond, J. M.: Geochemistry of the Amazon: 2. The influence of geology and weathering environment on the dissolved load, *Journal of Geophysical Research: Oceans*, 88, 9671–9688, <https://doi.org/10.1029/jc088ic14p09671>, 1983
- 940
- Torres, M. A., West, A. J., Li, G.: Sulphide oxidation and carbonate dissolution as a source of CO₂ over geological timescales, *Nature*, 507(7492), 346–349, <https://doi.org/10.1038/nature13030>, 2014
- Torres, M. A., West, A. J., Clark, K. E., Paris, G., Bouchez, J., Ponton, C., Adkins, J. F.: The acid and alkalinity budgets of weathering in the Andes–Amazon system: Insights into the erosional control of global biogeochemical cycles. *Earth and Planetary Science Letters*, 450, 381–391, <https://doi.org/10.1016/j.epsl.2016.06.012>, 2016
- 945
- Vallet, A. *Mouvements de fluides et processus de déstabilisation des versants alpins : Apport de l'étude de l'instabilité de Séchilienne*, Université de Franche-Comté, 2014
- 950
- Vallet, A., Bertrand, C., Mudry, J., Bogaard, T., Fabbri, O., Baudement, C., Régent, B.: Contribution of time-related environmental tracing combined with tracer tests for characterization of a groundwater conceptual model: a case study at the Séchilienne landslide, western Alps (France), *Hydrogeology Journal*, 23(8), 1761–1779, <https://doi.org/10.1007/s10040-015-1298-2>, 2015a
- 955
- Vallet, A., Charlier, J. B., Fabbri, O., Bertrand, C., Carry, N., Mudry, J.: Functioning and precipitation-displacement modelling of rainfall-induced deep-seated landslides subject to creep deformation, *Landslides*, 13, 653–670, <https://doi.org/10.1007/s10346-015-0592-3>, 2015b
- Vengeon, J. M.: *Déformation et rupture des versants en terrain métamorphique anisotrope : Apport de l'étude des Ruines de Séchilienne*, Université Joseph-Fourier - Grenoble I, 1998
- 960
- Vengeon, J.-M., Couturier, B., Antoine, P.: Déformations gravitaires post glaciaires en terrains métamorphiques. Comparaison des indices de déformation du versant sud de la Toura (Saint-Christophe-en-Oisans, France) avec le phénomène de rupture interne du versant sud du Mont Sec (Séchilienne, France), *Bulletin of Engineering Geology and the Environment*, 57(4), 387–395, <https://doi.org/10.1007/s100640050062>, 1999
- 965



Woods, T. L., Fullagar, P. D., Spruill, R. K., Sutton, L. C.: Strontium isotopes and major elements as tracers of ground water evolution: example from the Upper Castle Hayne Aquifer of North Carolina, *Ground Water*, 38(5), 762–771, <https://doi.org/10.1111/j.1745-6584.2000.tb02712.x>, 2000

970

Zeebe, R. E. and Wolf-Gladrow, D. A.: *CO₂ in Seawater: Equilibrium, Kinetics, Isotopes*, edited by Elsevier Oceanography Series, Amsterdam, 65, 2001.

975